Global Magnetohydrodynamics – A Tutorial

Joachim Raeder[1]

Institute of Geophysics and Planetary Physics, University of California, Los Angeles, USA

Remark: This is the web version (two-column, smaller figures, smaller margins, some corrections and additions) of the paper in *Space Plasma Simulation*, edited by: J. Büchner, C. T. Dum, and M. Scholer, Lecture Notes in Physics **615**, Springer Verlag, Berlin, 2003. ISBN 3-540-00698-2.

1 Introduction

Global modeling of geospace, that is, of the magnetosphere-ionosphere-thermosphere system, began about 20 years ago with the first simple magnetohydrodynamic (MHD) models of the solar wind - magnetosphere interaction [42,48]. It is thus a relatively young discipline compared to, for example, the modeling of the atmosphere. However, over this comparatively short period enormous progress has been made. While the first models were two-dimensional, it was soon realized that the magnetosphere is intrinsically three-dimensional, and such models appeared soon thereafter [18,55]. The next big step was the inclusion of electrodynamic ionosphere models that provided the closure of field-aligned currents (FACs) and the connection between magnetospheric and ionospheric convection [23,38,61,69,82]. These model extensions followed the realization that the ionosphere might, at least in part, control magnetospheric convection, and thus the magnetospheric dynamics in general. At this stage, the models were largely used to reproduce the large scale magnetospheric morphology and to investigate basic physical processes. However, it was not clear whether or not the model results and the underlying assumptions of magnetohydrodynamics were even correct, although they seemed to give correct answers for some parameters, for example the bow shock and magnetopause standoff distance. The ISTP program brought the first direct comparisons of model results with *in situ* measurements [25,26,66]. Since then there has been a flurry of model-data comparisons; too many to mention them all here. However, there have been several activities in which systematic comparisons were made, in particular the NSF/GEM convection challenge (see [50] and other articles in that issue) and the NSF/GEM substorm challenge (see [67] and other articles in that issue.) These studies have been particularly useful to assess the capabilities and limitations of current state-of-the-art models, that is, they (and other studies) have shown that global geospace models have now truly predictive capabilities. However, they have also shown deficiencies in many areas that require continued model development. Nevertheless, the models have become sufficiently efficient and sophisticated that they are now considered for use in the applications branch of space science – operational space weather forecasting.

In the following we discuss the physical and numerical foundation of global modeling, the coupling of different regions and processes, and examples of global simulations of substorm and storm events.

2 Global modeling – things to consider

Ideally, the magnetosphere-ionosphere system should be modeled using the Vlasov equations, i.e., the collisionless Boltzmann equations for the plasma species together with Maxwell's equations for the fields. Because this is impractical given the limited computer resources, the magnetohydrodynamic (MHD) equations are commonly used as the basis of a numerical model. Although the MHD equations appear relatively simple at a first glance, the development of efficient and accurate numerical algorithms for their solution is a formidable task that has not yet come to conclusion. For magnetosphere modeling the problem is exacerbated by the presence of multiple spatial and temporal scales. Therefore numerous different approaches have been developed, and the existing models differ in many respects. However, a number of issues is common to all models, and we discuss in the following their relevance and the advantages and disadvantages of various approaches.

2.1 Simulation Geometry and Numerical Grids

Any large-scale simulation starts with the choice of a numerical grid and the associated numerical methods. In the case of global simulations of Earth's magnetosphere the simulation boundaries should be well within supermagnetosonic flows, i.e., generally $\geq 18\ R_E$ from Earth on the sunward side, $\geq 200\ R_E$ in the tailward direction, and $\geq 50\ R_E$ in the transverse directions. However, these values are only a guide. For example, if the solar wind magnetosonic Mach number is very low the bow shock can move to several 10's of R_E upstream, in which case the sunward boundary must be farther away from Earth to keep the bow shock within the simulation domain.

There is a variety of choices for numerical grids. However, none of them is optimal and they all have their distinct advan-

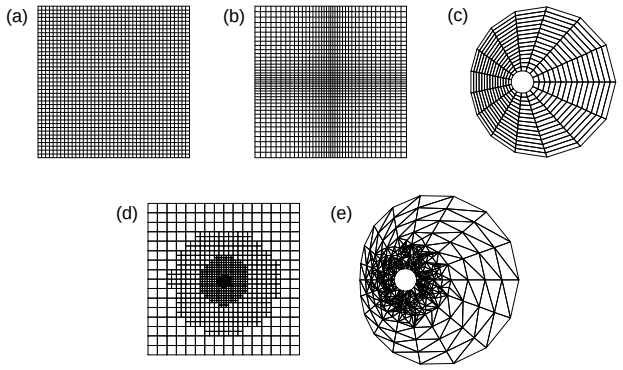

Fig. 1. Several common choices for numerical grids: **(a)** a uniform Cartesian grid, **(b)** a stretched Cartesian grid, **(c)** a non-Cartesian grid with Cartesian topology, **(d)** a structured adaptive grid, **(e)** a unstructured grid

tages and disadvantages. Consequently, virtually all possible grid approaches have been used to some extent.

Uniform Cartesian grids, like the one shown in Fig. 1a provide lowest programming overhead, lowest computing overhead, essentially no memory overhead, easiest parallelization, and near perfect load balancing for parallelized computation [55,89,56]. The major drawback is that such grids are not adapted to the solution. Consequently computational resources are wasted where they are not needed (in regions where the solutions are smooth) while other regions are under resolved, for example, sharp gradients and shocks.

Stretched Cartesian grids like the one shown in Fig. 1b can be better adapted to the solution, while maintaining essentially all of the advantages of a uniform Cartesian grid [61,84]. In the case of global magnetospheric simulations such a grid can actually be quite well adapted, providing high resolution in the X (sun-Earth) direction at the bow shock and the magnetopause, high resolution in the Z direction in the tail plasma sheet, and substantially lower resolution almost everywhere else. Consider a typical simulation box that is $300\times100\times100$ R_E^3 = 3×10^6 R_E^3 large. At a uniform 0.25 R_E resolution such a grid would require 1.92×10^8 cells, whereas a stretched Cartesian grid can achieve a 0.25 R_E resolution in the critical parts of the magnetosphere with $\sim$1-2$\times10^6$ cells. Thus, a stretched Cartesian grid requires about two orders of magnitude less computational resources. Such a grid is used, for example, in the UCLA code [61,69,65].

Grids as shown in Fig. 1c (non-Cartesian, but with Cartesian topology) are irregular but still with a regular connectivity between grid cells. This allows the grid better to be adapted to the solution with only small overhead in computation, however, post-processing and visualization becomes significantly more difficult. The Lyon-Fedder-Mobarry (LFM) code [49,24] uses such a grid.

A relatively new gridding strategy is based on overlaying grid patches with increasingly smaller resolution, such as shown in Fig. 1d. This approach is often call "structured adaptive mesh refinement" (SAMR) when combined with the dynamical adaptation of the grid to the solution, that is, grid patches are created and destroyed as the solution evolves in time [10,9]. The ratio of the gridsize between different *levels* in the grid hierarchy is a fixed integer (usually 2 or 4), and so is the timestep. Different refinement strategies are possible, like a block structure in which all patches are of the same size and ordered in a tree (for example, the BATS'R'US code of the Michigan group [60,29]). SAMR promises the most accurate solutions for a given number of grid cells. However, SAMR incurs substantial programming and computer overhead. Parallelization and load balancing of SAMR codes is extremely difficult.

Unstructured grids, like the one shown in Fig. 1e are suitable for finite element (FE) and finite volume (FV) methods. They are often constructed from triangles (in 2d) or tetrahedrons (in 3d), but other basic building blocks are also possible. Despite their geometrical flexibility, unstructured grids are rarely used in plasma simulation because of their high programming and computational overhead and because of the difficulty to parallelize such codes.

2.2 The Governing Equations

Although the magnetohydrodynamic (MHD) equations are often under scrutiny when applied to space plasmas, experience has proven that they are adequate in many situations where the spatial scale of interest is larger than the ion gyroradius and the ion inertial scales, and the temporal scale is longer than the ion gyroperiod. In assessing the validity of the MHD equations one must consider that they are *conservation equations*. Specifically, MHD describes the conservation of mass, momentum, energy, and magnetic flux. As far as the plasma is concerned the only significant underlying assumption is that the velocity distribution functions of the plasma constituents are only a function of $|\mathbf{v}-\mathbf{v}_d|$ in phase space, where $\mathbf{v}_d$ is the drift speed (first moment of the distribution). This is trivially fulfilled for a Maxwellian distribution and causes all moments higher than the scalar pressure to vanish (in the case of a Maxwellian distribution), or at least to decouple [8]. Violations of the $f(\mathbf{v}-\mathbf{v}_d)$=$f(|\mathbf{v}-\mathbf{v}_d|)$ assumption are mostly mild in large parts of the magnetosphere. However, they can be significant in the ring current, in regions of strong diffusion, and possibly in the plasma sheet. In places where such deviations from a symmetric distribution occur higher order moments, for example the heat flux tensor, come into play. The correct closure of the equation set becomes then becomes an issue [34,35]. In some cases it is possible to augment the MHD equations appropriately (for example by adding anomalous diffusion terms); however, in other cases (for example, the ring current) a different formalism is indicated [90].

The MHD equations can be written in different forms, which are all mathematically equivalent, but generally lead to different numerical methods. In the following, the symbols

have their usual meaning, e.g., $\mathbf{B}$ and $\mathbf{E}$ are the magnetic and electric field, respectively, $\mathbf{v}$ is the plasma velocity, ρ is the density, p is the pressure, $\mathbf{j}$ is the current density, η is a resistivity, $\underline{\underline{\mathrm{I}}}$ is the unit tensor, and γ is the ratio of specific heats.

Non-conservative (primitive variable) formalism:

$$\frac{\partial \rho}{\partial t} = -\nabla\cdot(\rho\mathbf{v}) \tag{1a}$$

$$\frac{\partial \mathbf{v}}{\partial t} = -(\mathbf{v}\cdot\nabla)\mathbf{v} - \frac{1}{\rho}(\nabla p - \mathbf{j}\times\mathbf{B}) \tag{1b}$$

$$\frac{\partial p}{\partial t} = -(\mathbf{v}\cdot\nabla)p - \gamma p\nabla\cdot\mathbf{v} \tag{1c}$$

$$\frac{\partial \mathbf{B}}{\partial t} = -\nabla\times\mathbf{E} \tag{1d}$$

$$\nabla\cdot\mathbf{B} = 0 \tag{1e}$$

$$\mathbf{E} = -\mathbf{v}\times\mathbf{B} + \eta\mathbf{j} \tag{1f}$$

$$\mathbf{j} = \nabla\times\mathbf{B} \tag{1g}$$

The primitive variable formulation leads to numerical schemes that do not strictly conserve momentum and energy, even in the hydrodynamic case. Such schemes do not guarantee correct shock speeds and correct jump conditions at discontinuities [41]. Furthermore, the convective derivative $(\mathbf{v}\cdot\nabla)$ is difficult to treat numerically. Although the use of the primitive variable formulation leads to algorithms with low memory requirements, its use should be avoided because much better approaches are available.

Full conservative formalism:

$$\frac{\partial \rho}{\partial t} = -\nabla\cdot(\rho\mathbf{v}) \tag{2a}$$

$$\frac{\partial \rho\mathbf{v}}{\partial t} = -\nabla\cdot\left\{\rho\mathbf{v}\mathbf{v} + \underline{\underline{\mathrm{I}}}(p + \frac{B^2}{2}) - \mathbf{B}\mathbf{B}\right\} \tag{2b}$$

$$\frac{\partial U}{\partial t} = -\nabla\cdot\left\{(U+p)\mathbf{v} + \mathbf{E}\times\mathbf{B}\right\} \tag{2c}$$

$$\frac{\partial \mathbf{B}}{\partial t} = -\nabla\times\mathbf{E} \tag{2d}$$

$$\nabla\cdot\mathbf{B} = 0 \tag{2e}$$

$$\mathbf{E} = -\mathbf{v}\times\mathbf{B} + \eta\mathbf{j} \tag{2f}$$

$$\mathbf{j} = \nabla\times\mathbf{B} \tag{2g}$$

$$U = \frac{p}{\gamma-1} + \frac{\rho v^2}{2} + \frac{B^2}{2} \tag{2h}$$

The full conservative formulation allows the application of conservative finite difference schemes that strictly conserve mass (ρ), momentum (ρv), energy (U), and magnetic flux. This formulation is therefore always preferable. It may lead, however, to difficulties in low β regions ($\beta = p/(B^2\mu_0)$ is the ratio of the plasma pressure to the magnetic field pressure) where the pressure becomes the difference of two large numbers. Numerical errors can then cause nonphysical negative pressures. A semi-conservative form of the equations may then be more appropriate.

Gas dynamic conservative (semi-conservative) formalism:

$$\frac{\partial \rho}{\partial t} = -\nabla\cdot(\rho\mathbf{v}) \tag{3a}$$

$$\frac{\partial \rho\mathbf{v}}{\partial t} = -\nabla\cdot(\rho\mathbf{v}\mathbf{v} + p\underline{\underline{\mathrm{I}}}) + \mathbf{j}\times\mathbf{B} \tag{3b}$$

$$\frac{\partial e}{\partial t} = -\nabla\cdot(\{e+p\}\mathbf{v}) + \mathbf{j}\cdot\mathbf{E} \tag{3c}$$

$$\frac{\partial \mathbf{B}}{\partial t} = -\nabla\times\mathbf{E} \tag{3d}$$

$$\nabla\cdot\mathbf{B} = 0 \tag{3e}$$

$$\mathbf{E} = -\mathbf{v}\times\mathbf{B} + \eta\mathbf{j} \tag{3f}$$

$$\mathbf{j} = \nabla\times\mathbf{B} \tag{3g}$$

$$e = \frac{\rho v^2}{2} + \frac{p}{\gamma-1} \tag{3h}$$

The semi-conservative formulation allows for difference schemes that numerically conserve of mass (ρ), momentum (ρv), and plasma energy (e), but with no strict conservation of total energy. On the other hand, low β regions pose no difficulty. This approach can be combined with a full conservative scheme by integrating both energy equations (2c) and (3c) and using a 'β switch', as suggested by Balsara and Spicer [7].

The above equations are normalized with arbitrary normalization factors (3 of them are independent.) This is possible because the MHD equations have no intrinsic length or time scale. This changes, however, when Earth's dipole is introduced, which essentially provides the normalization of the magnetic field.

Frequently the ideal (that is, non-dissipative) MHD equations need to be augmented with a term for anomalous resistivity η. While any numerical code produces numerical resistivity, enough to enable magnetic reconnection, in some circumstances this may not be sufficient. A notable example is the dynamical evolution of substorms [68]. Although the precise mechanisms that cause anomalous diffusion are not well known, it is generally believed that anomalous diffusion is a function of the local current density, thus a suitable parametrization is given by, for example:

$$\eta = \alpha j'^2 \quad \text{if} \quad j' \geq \delta, \quad 0 \text{ otherwise} \tag{4}$$

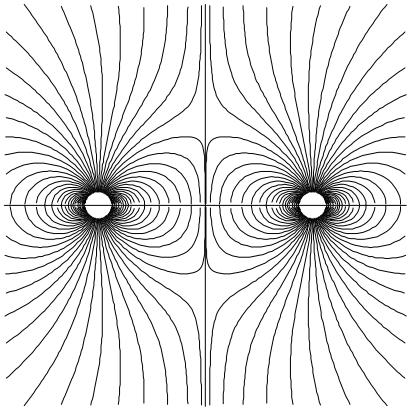

Fig. 2. Initial magnetic field constructed with a mirror dipole

$$j' = \frac{|j|\Delta}{|B| + \varepsilon} \tag{5}$$

where j' is a normalized local current density, Δ is the grid spacing, and δ and α are empirical constants [65].

2.3 Boundary and initial conditions

The outer boundary conditions of the simulation domain are relatively straight-forward. However, the inner boundary, where the magnetospheric field meets the ionosphere, is much more involved.

Sunward side: The boundary conditions can be either arbitrary (fixed or time dependent), or measured solar wind data can be used. However, solar wind data are usually limited to one (or at best a few) solar wind monitors, thus there is very little knowledge of the true 3d structure of the solar wind. This leads to a problem with B_x: The three-dimensional structure of the solar wind needs to be known because

$$\nabla \cdot \mathbf{B} = 0 \qquad \Longleftrightarrow \qquad \mathbf{n} \cdot (B_{upstream} - B_{downstream}) = 0, \tag{6}$$

across any discontinuity in the IMF. This implies that $B_x = B_n$ cannot change if solar wind parameters are independent of Y and Z (simple extrapolation). A possible solution is to find the predominant normal vector $\mathbf{n}$ in the sense that all solar wind discontinuities during some time period are only a function of $\mathbf{n}$. This is difficult with a single solar wind monitor; however, boundary normal methods (for example, the minimum variance method [77,78]) can be applied.

On all other sides: Here, free flow conditions can be applied, i.e.,

$$\frac{\partial \Psi}{\partial \mathbf{n}} = 0 \tag{7}$$

for all variables Ψ, except for the normal magnetic field which must be derived from the $\nabla \cdot \mathbf{B} = 0$ condition and which must be consistent with the numerical scheme.

Magnetic field initial conditions: The magnetic field can be initialized by the superposition of dipole with mirror dipole to create $B_x = 0$ surface sunward of Earth (see Fig. 2). The field on sunward side is then replaced with the initial solar wind field, providing a $\nabla \cdot \mathbf{B} = 0$ transition.

Plasma initial conditions: The initial plasma conditions are usually given by a cold (5000 ^{0}K), tenuous (0.1cm^{-3}), uniform plasma. From the start of the simulation it takes about 0.5-1 hour real time for the magnetosphere to form. However, the magnetosphere can have a substantial memory of prior conditions (possibly many hours), thus it is advisable to provide at least a few hours lead time from the start of a simulation up to a specific event.

2.4 MHD numerics

Time differencing Consider the model equation:

$$\frac{\partial U}{\partial t} = -\nabla \cdot \mathbf{F}(U) \tag{8}$$

which is representative for the plasma part of the conservative or semi-conservative MHD equations (2,3).

Fairly simple difference schemes can be applied to the time derivative with second order accuracy (that is, numerical errors are proportional to Δt^2; more on that later), for example, the explicit predictor-corrector scheme:

$$\begin{aligned} U^{n+\frac{1}{2}} &= U^n - \frac{1}{2}\Delta t \nabla \cdot \mathbf{F}(U^n), \\ U^{n+1} &= U^n - \Delta t \nabla \cdot \mathbf{F}(U^{n+\frac{1}{2}}) \,, \end{aligned} \tag{9}$$

or the explicit leap-frog scheme:

$$U^{n+1} = U^{n-1} - 2\Delta t \nabla \cdot \mathbf{F}(U^n, U^{n-1}) \,. \tag{10}$$

These schemes are generally accurate enough, sufficiently simple, and require moderate storage. However, they suffer from a stability requirement (the Courant-Friedrichs-Levy, or CFL criterion [76]) that limits the stable time step to Δt_{max}:

$$\Delta t_{max} \leq \delta \frac{\min(\Delta x, \Delta y, \Delta z)}{|\mathbf{v}| + v_{MS}} \,, \tag{11}$$

where δ is a constant of the order $O(1)$. The CFL criterion can be very restrictive because $\Delta t < \Delta t_{max}$ must be satisfied everywhere in the simulation domain, not just locally. In some parts of the magnetosphere the Alfvén speed can become very large, severely limiting the stable time step. It is possible to apply the 'Boris correction' [13,17] or some variant thereof which limits the Alfvén speed. This essentially entails the simultaneous reduction of the $\mathbf{J}\times\mathbf{B}$ and the perpendicular (to the magnetic field) component of the ∇p force in regions where the Alfvén speed would be too high. A judicious choice of the reduction

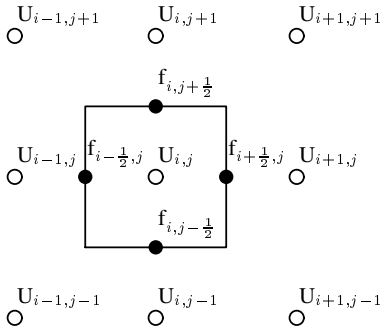

Fig. 3. Variable placement of the numerical fluxes

factor allows for much larger time steps without any adverse effects on the solutions.

Implicit time differencing schemes, where the right hand side involves variables at time level $n+1$:

$$U^{n+1} = U^n - \Delta t \nabla \cdot \mathbf{F}(U^{n+1}, U^n, U^{n-1}, \ldots) \tag{12}$$

can be unconditionally stable, but generally require the solution of large linear systems, which is computationally very expensive and generally impractical.

Spatial discretization The spatial discretization of the MHD equations is much more difficult than the time discretization. There are basically four different approaches: a) finite differences (FD), b) finite volume (FV) methods, which usually reduce to FD methods on Cartesian grids, c) finite element (FE) methods, and d) spectral methods.

Since FD methods are most widely used in global magnetosphere models we restrict the discussion to these in the following. However, many FD concepts carry over to the other methods as well. More specifically, we focus on the discussion of *conservative difference schemes* since these are most suitable for global simulations.

Consider again the model equation, but this time with emphasis on the right hand side:

$$\frac{\partial U}{\partial t} = -\nabla \cdot \mathbf{F}(U) \tag{13}$$

where U is some variable and $\mathbf{F}(U)$ the flux associated with that variable. Introduce a regular Cartesian grid (in 2d) where the cell centers are at $x_i = i\Delta x, i = 1, \ldots$ and $y_j = j\Delta y, j = 1, \ldots$ and the cell corners are at $(x_{i+1/2,j+1/2}, y_{i+1/2,j+1/2})$. Discretize the right hand side of equation (13) as:

$$\begin{aligned} \frac{\partial U}{\partial t} = &- (f_{i+\frac{1}{2},j}(U) - f_{i-\frac{1}{2},j}(U))/\Delta x \\ &- (f_{i,j+\frac{1}{2}}(U) - f_{i,j-\frac{1}{2}}(U))/\Delta y \,, \end{aligned} \tag{14}$$

where we introduced the *numerical fluxes* $f_{i+\frac{1}{2},j}$ and $f_{i,j+\frac{1}{2}}$, which are functions of the grid values:

$$f_{i+\frac{1}{2},j} = G_x(\ldots, U_{i-1,j}, U_{i,j}, U_{i+1,j}, \ldots) \tag{15}$$

$$f_{i,j+\frac{1}{2}} = G_y(\ldots, U_{i,j-1}, U_{i,j}, U_{i,j+1}, \ldots) \,, \tag{16}$$

and which must be *consistent* with the physical flux $\mathbf{F}(U)$ in the following sense:

$$\mathbf{G}(U, \ldots, U, U, \ldots, U) = \mathbf{F}(U) \,. \tag{17}$$

Writing equation (13) in integral form:

$$\frac{\partial}{\partial t} \int_V U dV = \int_S \mathbf{F} d\mathbf{s} \,, \tag{18}$$

where V is an arbitrary, simply connected volume, S its surface, and $\mathbf{s}$ its surface normal, it is now easy to see that the variable U is globally conserved. In Fig. 3 this volume is taken to be one cell (i, j). Considering the cell that contains $U_{i,j}$, any change of $U_{i,j}$ must be opposite to the sum of the changes of the four surrounding cell variables $U_{i-1,j}$, $U_{i+1,j}$, $U_{i,j-1}$, $U_{i,j+1}$ caused by the flow of U through the cell boundaries. Thus, the sum of $\partial U_{i,j}/\partial t$ over the entire grid is zero, except for the fluxes through the physical boundaries.

Using the discretization (14) only guarantees the global conservation of the quantity U. The accuracy of the approximation is determined by the construction of the numerical fluxes $f_{i+\frac{1}{2},j}$ and $f_{i,j+\frac{1}{2}}$.

A few popular schemes are listed in the following; for simplicity we drop the second dimension:

- The second order central scheme:

$$f_{i+\frac{1}{2}} = \frac{1}{2}(F(U_i) + F(U_{i+1})) \tag{19}$$

- The fourth order central scheme:

$$f_{i+\frac{1}{2}} = \frac{7}{12}(F(U_i) + F(U_{i+1})) - \frac{1}{12}(F(U_{i-1}) + F(U_{i+2})) \tag{20}$$

- The Lax scheme:

$$f_{i+\frac{1}{2}} = \frac{1}{2}(F(U_i) + F(U_{i+1})) - \frac{1}{2}(U_{i+1} - U_i) \tag{21}$$

- The two step Lax Wendroff scheme: Use Lax scheme for predictor, and second order central for corrector.
- The Rusanov scheme:

$$\begin{aligned} f_{i+\frac{1}{2}} = &\frac{1}{2}(F(U_i) + F(U_{i+1})) \\ &- \frac{1}{4}(|v_i| + |v_{i+1}| + c_i + c_{i+1})(U_{i+1} - U_i) \end{aligned} \tag{22}$$

  where c is the sound speed.
- The Godunov type schemes solve a Riemann problem (i.e. the decay of a step function into waves) at the cell interface $i+\frac{1}{2}$ and compute the fluxes directly from the wave propagation (see e.g. [93,20] and references therein.) This is very accurate for gas-dynamics, but difficult for MHD because the system of equations involves a degenerate eigenvector related to $\nabla \cdot \mathbf{B} = 0$ [19].

Error terms The error terms associated with the spatial discretization can be found via a Taylor series expansion:

$$\Delta x\frac{\partial U}{\partial t} = -(f_{i+\frac{1}{2}} - f_{i-\frac{1}{2}}) + a_1(\Delta x)^2\frac{\partial^2}{\partial x^2}F(U) + b_1(\Delta x)^3\frac{\partial^3}{\partial x^3}F(U) + a_2(\Delta x)^4\frac{\partial^4}{\partial x^4}F(U) + b_2(\Delta x)^5\frac{\partial^5}{\partial x^5}F(U) + \dots \quad (23)$$

The coefficients a_1, b_1, etc. depend of course on the choice of the numerical flux scheme. The error terms associated with even derivatives cause numerical *diffusion*, that is, they tend to smear out the solution, in particular at discontinuities where the derivatives of the solution become large. Conversely, the error terms associated with odd derivatives cause numerical *dispersion*, which manifests itself mostly by ripples and under/overshoots near discontinuities. Dispersion is in a certain sense the worst enemy, because it may lead to nonphysical solutions, such as negative density or pressure.

Ideally, one wants to construct numerical fluxes that minimize the error terms. The order of a scheme is defined as the smallest order of the derivative with non-vanishing coefficient minus one, for example, a third order scheme will only have error terms proportional to the fourth and higher derivatives of the solution. First order schemes are thus primarily diffusive (with second order diffusion terms). All symmetric central schemes have no diffusion at all, that is, all a terms vanish. Although that may seem a desirable property, the dispersion of these schemes makes them virtually useless for any application that involves shocks, such as the magnetosphere, because of extreme over- and under-shoots near the shock and other discontinuities.

A more desirable property of the numerical scheme is therefore *monotonicity*. A scheme is called *monotone* if it lets no *new* extrema develop in the solution. Of course, there may be physically relevant extrema in the solution; however, one can show that, at least in 1d, the number of extrema is non-increasing.

Unfortunately, *Harten's Lemma* [32] states that a monotone scheme is at most first order accurate. Thus, the price for global monotonicity seems to be the large diffusion of first order schemes, such as the Lax or the Rusanov scheme. Harten (and others) also proposed the solution to this dilemma, which essentially amounts to the *hybridization* of the numerical fluxes. Instead of using one and the same scheme in the entire domain, a first order scheme is employed where the gradients in the solutions are large, while in those regions where the solution is smooth a higher order scheme is used. In its simplest form the numerical flux is then computed as follows:

$$f_{i+\frac{1}{2}} = \theta_{i+\frac{1}{2}} f^h_{i+\frac{1}{2}} + (1-\theta_{i+\frac{1}{2}}) f^l_{i+\frac{1}{2}} \quad (24)$$

where f^l is a low order (for example Rusanov) flux, and f^h is a high order (for example second or fourth order central) flux [33,95]. The conservation properties of the scheme are preserved and do not depend on which fluxes are used and how they are combined. Note that flux hybridization is not possible for the non-conservative equations.

The switch function θ acts as a *Flux Limiter* and is generally a function of gradients in the solution, e.g., a function of the grid values surrounding $i+\frac{1}{2}$. The hybridization procedure is not always written in the above stated form and the term *Flux limiter* is often used in a somewhat different, but related context [37]. However, the principle is always the same. There is no optimal choice for a flux limiter, and numerous schemes have been developed. Most notable among them are the original hybrid method [33], *Flux Corrected Transport (FCT)* [14,94,95,21], *Total Variance Diminishing (TVD)* schemes [31,81,91,92], *Essentially Non-oscillatory (ENO)* schemes [43,39], and the *Van Leer* flux limited schemes [85–87].

Magnetic flux conservation A particular difficulty of MHD simulations (as opposed to hydrodynamic simulations) is the conservation of magnetic flux, expressed as the Maxwell equation $\nabla\cdot\mathbf{B}$=0. $\nabla\cdot\mathbf{B}$=0 is an initial condition since $\nabla\cdot\mathbf{B}$ is conserved by Faraday's law:

$$\nabla\cdot\frac{\partial\mathbf{B}}{\partial t} = \frac{\partial(\nabla\cdot\mathbf{B})}{\partial t} = -\nabla\cdot\nabla\times\mathbf{E} = 0 \quad (25)$$

Most numerical schemes do not *a priori* preserve $\nabla\cdot\mathbf{B}$. For such schemes the accumulation of $\nabla\cdot\mathbf{B}$ can lead to serious errors, in particular spurious parallel acceleration, wrong magnetic topology (field lines that are not closed), and significant errors in the shock jumps [16,83]. There are a few methods to "clean" the magnetic field of monopoles, for example the projection method:

$$\nabla^2\Psi = -(\nabla\cdot\mathbf{B}) \quad (26)$$

produces a monopole potential that can be used as a correction:

$$\mathbf{B}' = \mathbf{B} + \nabla\Psi \quad (27)$$

Note that the projection method requires the solution of a Poisson equation on the global grid which can be quite costly. Because the numerical solution of this equation has errors as well, the projection method can only achieve $\nabla\cdot\mathbf{B} = 0$ to a certain order in the gridspacing [83].

An alternative approach is to modify the MHD equations in such a way that $\nabla\cdot\mathbf{B}$ becomes a convected quantity [60,29]:

$$\frac{d(\nabla\cdot\mathbf{B})}{dt} = 0 \quad (28)$$

This approach does not guarantee any limit on the accumulation of $\nabla\cdot\mathbf{B}$ and may also lead to the violation of the shock jumps [83].

A preferable approach is to use a scheme that conserves magnetic flux *a priori*. Such a scheme was first introduced by Evans and Hawley [22] in the context of MHD simulations. Flux conservation is achieved by using staggered grids for the

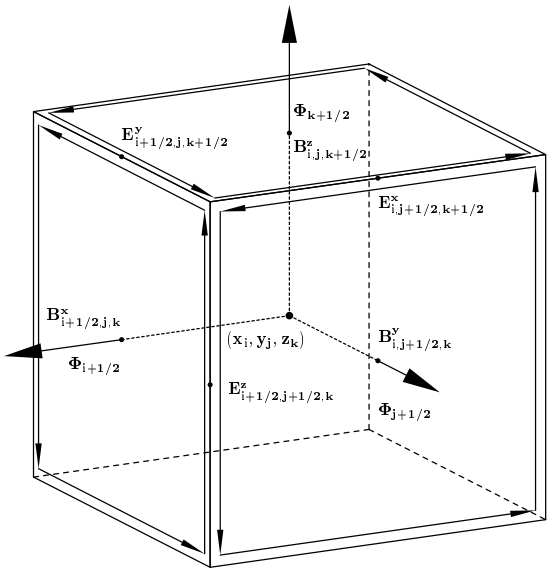

Fig. 4. Variable placement on a staggered grid for magnetic flux conserving integration of Faraday's law. The arrows along the cell edges indicate the electric field contributions in the magnetic field time integration step

magnetic and electric field, such that the magnetic field components are placed on the center of cell faces:

$$(B_x)_{i+\frac{1}{2},j,k}, (B_y)_{i,j+\frac{1}{2},k}, (B_z)_{i,j,k+\frac{1}{2}} ,$$

and the electric field (the numerical flux for the **B** integration) on the centers of the cell edges:

$$(E_x)_{i,j+\frac{1}{2},k+\frac{1}{2}}, (E_y)_{i+\frac{1}{2},j,k+\frac{1}{2}}, (E_z)_{i+\frac{1}{2},j+\frac{1}{2},k} ,$$

as indicated in Fig. 4. The magnetic field time integration becomes then particularly simple, for example:

$$\frac{\partial}{\partial t}(B_x)_{i+\frac{1}{2},j,k} = \tag{29}$$
$$\{(E_y)_{i+\frac{1}{2},j,k+\frac{1}{2}} - (E_y)_{i+\frac{1}{2},j,k-\frac{1}{2}}\}/\Delta z$$
$$-\{(E_z)_{i+\frac{1}{2},j+\frac{1}{2},k} - (E_z)_{i-\frac{1}{2},j+\frac{1}{2},k}\}/\Delta y .$$

and analogously for B_y and B_z. By advancing the field components in this way on all 6 cell faces and summing up it follows:

$$\frac{\partial}{\partial t}\int\int_{cell} \Phi df = \Delta y \Delta z (\frac{\partial B_x}{\partial t})_{i-\frac{1}{2}}$$
$$+\Delta y \Delta z (\frac{\partial B_x}{\partial t})_{i+\frac{1}{2}} + \Delta x \Delta z (\frac{\partial B_y}{\partial t})_{j+\frac{1}{2}} + \ldots$$
$$= \{((E_y)_{i+\frac{1}{2},j,k+\frac{1}{2}} - (E_y)_{i+\frac{1}{2},j,k+\frac{1}{2}}) +$$
$$((E_y)_{i+\frac{1}{2},j,k-\frac{1}{2}} - (E_y)_{i+\frac{1}{2},j,k-\frac{1}{2}}) + \ldots\}\Delta x \Delta y \Delta z = 0 , \tag{30}$$

and thus the combined magnetic flux Φ through all 6 cell faces remains unchanged (Φ = const.) during the time integration, as required by equation (25). Note that the field can be divergence-free initialized by using a vector potential **A** in place of **E** [22].

Coordinate transformation for stretched Cartesian grids It is particularly simple to integrate the equations on a stretched Cartesian grid. Let the grid coordinates be given by analytic functions of the grid indices (i, j, k), that is: $x = x(i)$, y=$y(j)$, z=$z(k)$, then:

$$\frac{\partial}{\partial x}F(x,y,z) == \frac{\partial F}{\partial i}\frac{\partial i}{\partial x} = \frac{\partial F}{\partial i}\left(\frac{\partial x}{\partial i}\right)^{-1} , \tag{31}$$

and analogously for y and z derivative. The derivatives on the regular equidistant (i,j,k) grid need then only be multiplied with the appropriate geometric factors:

$$\frac{\partial}{\partial x}F(x,y,z) = \frac{\partial F}{\partial i}\left(\frac{\partial x}{\partial i}\right)^{-1} \tag{32}$$

$$\frac{\partial}{\partial y}F(x,y,z) = \frac{\partial F}{\partial j}\left(\frac{\partial y}{\partial j}\right)^{-1} \tag{33}$$

$$\frac{\partial}{\partial z}F(x,y,z) = \frac{\partial F}{\partial k}\left(\frac{\partial z}{\partial k}\right)^{-1} . \tag{34}$$

3 Coupling of different regions and processes

Modeling the magnetosphere extends beyond solving the MHD equations. At a minimum, the MHD model needs an inner boundary at which FACs generated in the magnetosphere close through the resistive ionosphere. This process is commonly implemented such that the MHD calculation only extends to within 3-4R_E from Earth. Within that boundary the FACs are mapped along dipole field lines into the ionosphere. At the ionosphere end a potential equation is solved on a sphere (or a section thereof) to yield the ionospheric convection potential [23]. The potential is then mapped back to the inner boundary of the MHD calculation where it is used as boundary condition for the flow and field integration ($\mathbf{v} = (-\nabla\Phi)\times\mathbf{B}/|B|^2$). This mapping is illustrated in Fig. 5.

Such a mapping typically covers latitudes from $\sim 58^0$ to 90^0. In the region between the ionosphere and the inner boundary of the magnetosphere the MHD equations are not solved. This is partly necessitated by the high Alfvén speeds in this region, and also by the fact that the relevant processes on these field lines are not well described by the MHD equations, but are for the most part of a kinetic nature.

The relevance of the ionosphere for magnetospheric dynamics is best explained by the limiting cases. In the case of a vanishing ionospheric potential Φ, equivalent to infinite ionospheric conductance, the electric field and the convection velocity will also vanish ($\Phi = 0 \longrightarrow \mathbf{E} = 0 \longrightarrow \mathbf{v} = 0$). Thus, there is no convection in the ionosphere and field lines are tied. Ultimately (on a time scale of less than one hour) magnetospheric convection has to cease as well. In the opposite case the conductance of the ionosphere is zero which means that no current can flow from the magnetosphere through the ionosphere ($j_\parallel \to 0$). In that case field lines slip free through the ionosphere

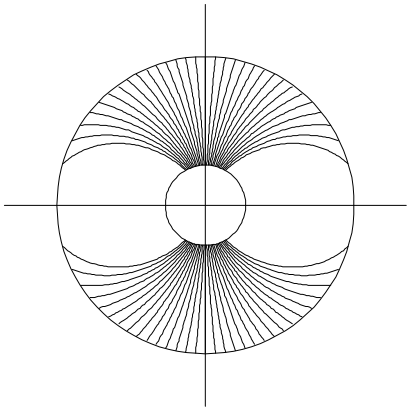

Fig. 5. Schematic of the field line mapping between the magnetosphere and the ionosphere

and the Earth (because the solid Earth's conductivity is small). Thus, magnetospheric convection can proceed uninhibited.

In reality the ionosphere has a finite conductance and field lines are dragged through the ionospheric plasma, dissipating energy that must be supplied from the magnetosphere via Poynting flux [58,79]. Thus, the ionosphere influences magnetospheric convection, and the primary controlling factor is the ionospheric conductance.

The magnetosphere-ionosphere coupling can be described either in a mechanical way, that is by calculating the stresses and motions of the ionospheric constituents (ions, electrons, and neutrals [80]), or by treating it as an electric circuit [88]. The latter approach is far easier to implement. Field-aligned currents are calculated at the magnetospheric boundary and used as input to the ionospheric potential equation. The polar ionosphere can be treated as a 2d shell to a very good approximation (because field lines are nearly radial), thus:

$$\nabla \cdot \underline{\underline{\Sigma}} \cdot \nabla \Phi = -j_{\parallel} \sin I \tag{35}$$

with the boundary condition Φ=0 at the magnetic equator. Because the ionosphere is a magnetized and partially ionized plasma the ionospheric conductance is a tensor [80], given by:

$$\underline{\underline{\Sigma}} = \begin{pmatrix} \Sigma_{\theta\theta} & \Sigma_{\theta\lambda} \\ -\Sigma_{\theta\lambda} & \Sigma_{\lambda\lambda} \end{pmatrix} \tag{36}$$

$$\Sigma_{\theta\theta} = \frac{\Sigma_P}{\sin^2 I} \quad , \quad \Sigma_{\theta\lambda} = \frac{\Sigma_H}{\sin I} \quad , \quad \Sigma_{\lambda\lambda} = \Sigma_P \tag{37}$$

where Σ_H is the Hall conductance, Σ_P is the Pedersen conductance, θ is the magnetic latitude, λ is the magnetic longitude, and I is the magnetic field inclination.

The potential calculation requires the specification of the ionospheric Hall and Pedersen conductance. These can either be assumed to be uniform (not a good assumption), be computed using empirical formulations, or be computed using a full-fledged ionosphere-thermosphere model.

The conductances are proportional to the ionospheric electron density (essentially E-region), which in turn is primarily given by solar EUV irradiance and precipitation of magnetospheric electrons. The conductance contribution of the former can be easily parameterized from measurements, for example as [54]:

$$\Sigma_H = F_{10.7}^{0.53}(0.81\cos\chi + 0.54\cos^{1/2}\chi) \tag{38}$$

$$\Sigma_P = F_{10.7}^{0.49}(0.34\cos\chi + 0.93\cos^{1/2}\chi) \tag{39}$$

where $F_{10.7}$ is the solar radio flux (used as a proxy for solar EUV radiation) and χ is the solar zenith angle. Magnetospheric electron precipitation is either diffuse (pitch angle scattering of hot magnetospheric electrons), or discrete (accelerated auroral electrons.) The former can be parameterized by:

$$F_E = n_e(kT_e/2\pi m_e)^{\frac{1}{2}} \qquad , \qquad E_0 = kT_e \tag{40}$$

where T_e and n_e are the magnetospheric electron temperature and density, respectively. F_E is the energy flux, and E_0 is the mean energy of the precipitating electrons. Discrete electron precipitation can be modeled using the Knight relation [40,59]:

$$\Delta\Phi = max(0, -j_{\parallel})/K \tag{41}$$

$$K = \frac{e^2 n_e}{\sqrt{2\pi m_e k T_e}} \tag{42}$$

$$F_E = \Delta\Phi_{\parallel} j_{\parallel} \qquad , \qquad E_0 = e\Delta\Phi_{\parallel} \tag{43}$$

where $\Delta\Phi$ is the parallel potential drop on an auroral field line. K^{-1} can be viewed as the resistance of the field line.

The Pedersen and Hall conductances can then be computed using empirical formulas, for example [74]:

$$\Sigma_P = [40E_0/(16 + E_0^2)]F_E^{1/2} \tag{44}$$

$$\Sigma_H = 0.45E_0^{5/8}\Sigma_P \tag{45}$$

or by feeding the precipitation parameters, along with the potential, into a large-scale ionosphere-thermosphere model which then computes the conductances self-consistently from the electron-neutral collisions. The latter approach has recently been taken by combining the UCLA magnetosphere-ionosphere (MI) code with the NOAA Coupled Thermosphere Ionosphere Model (CTIM, [28,70]).

The CTIM part of the coupled model is a global multi-fluid model of the thermosphere–ionosphere system with a long heritage [28]. CTIM solves both neutral and ion fluid equations self-consistently from 80 to 500 km for the neutral atmosphere and from 80 to 10,000 km for the ionosphere on a spherical grid with 2° latitude resolution and 18° longitude resolution. The thermosphere part solves the continuity equation, horizontal momentum equation, energy equation, and composition equations for the major species O, O_2, and N_2 on 15 pressure levels. The ionosphere model part solves the continuity equations,

ion temperature equation, vertical diffusion equations, and horizontal transport for H^+ and O^+, while chemical equilibrium is assumed for N_2^+, O_2^+, NO^+, and N^+. The horizontal ion motion is governed by the magnetospheric electric field. The coupled model includes about 30 different chemical and photo-chemical reactions between the species. CTIM's primary inputs are the solar UV and EUV fluxes (parameterized by the solar 10.7 cm radio flux), the tidal modes (forcing from below), auroral precipitation, and the magnetospheric electric field, each of which is usually taken from parameterized empirical models. CTIM provides several outputs that are of prime importance for space weather, for example, global two- and three-dimensional ionosphere and thermosphere state fields, like electron density, neutral density, neutral wind, chemical composition, NmF2, hmF2, and total electron content (TEC). A more thorough description of CTIM, including the detailed equations, reaction rates, and examples can be found in [28].

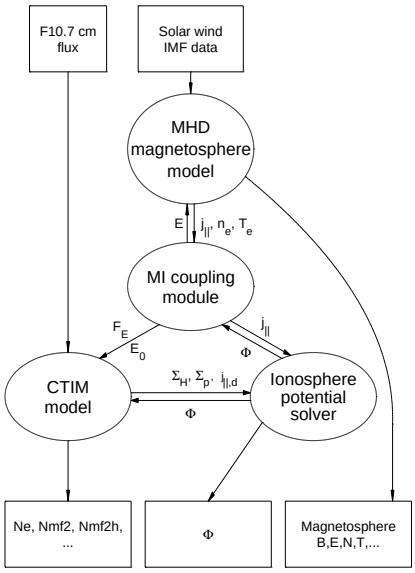

Fig. 6. Schematic showing the coupling between the UCLA magnetosphere-ionosphere model with the NOAA Coupled Thermosphere Ionosphere Model (CTIM)

The coupling of the models is schematically shown in Figure 6. The MI model provides the electron precipitation parameters and the magnetospheric field-aligned currents (FACs.) In turn, CTIM provides the ionospheric conductance and the ionospheric dynamo current to the MI model. Thus, as far as the MI model is concerned, we replace empirical conductance calculations [74] that was used in most prior studies with first-principle calculations and also account for the ionospheric dynamo effect. The latter effect is probably of minor importance in most situations, but may become significant during storm recovery [73]. With this coupling, CTIM is also driven with more realistic magnetospheric inputs and depends on fewer empirical parameters.

4 Examples: Substorms and storms

An important aspect of any kind of numerical modeling is to ensure the correctness of the model. Here, two issues come into play. First, one needs to verify that the model solves the underlying equations correctly. However, because numerical models compute only *approximations* to the underlying equations, the issue rather becomes to quantify the approximation errors. Ideally, this can be done by comparing model results with known analytic solutions. For global models, however, this approach has limitations because there are no known analytic solutions that even come close to the true complexity of the magnetosphere. Thus, much simpler analytic tests are usually conducted, for example, shock tube problems, magnetic field convection problems, equilibrium solutions, and checks of the conservation properties of the code (mass, momentum, energy, and magnetic flux). Such tests give some idea of how well an algorithm works, however, because of their simplicity they still leave open the possibility of serious errors in the simulation of the complex magnetosphere. The second issue involves the validity of the underlying equations themselves. Here, limited comparisons can be made with more sophisticated local models. For example, one can compare reconnection geometries and reconnection rates with those predicted by kinetic models. However, such comparisons are problematic because it is virtually impossible to set up test cases in a way that the boundary conditions for either model are the same. On the other hand, global models can be run with measured solar wind and IMF data as input and their results can then be compared with *in situ* observations. By doing so, both of the two issues above are addressed at the same time. If the simulation results match the *in situ* data well one can be confident that the equations are sufficient to describe the phenomena *and* that the numerical solution is sufficiently accurate. Inevitably, there will also be differences found between the simulation results and the data. Careful analysis of these differences, together with our theoretical understanding of the physical processes involved, will usually show if they are the result of numerical errors or the result of deficiencies in the underlying equations and assumptions. For example, the lack of ring current formation in global magnetosphere models is clearly caused by the simplifications inherent in the MHD equations which neglect the drift physics of the more energetic plasma populations. On the other hand, excessive reconnection rates may be the result of numerical effects like limited resolution or numerical diffusion.

Global geospace modeling is therefore most powerful if done in conjunction with data analysis. Very often it is impossible to draw solid conclusion from single (or a few) spacecraft observations. For example, a spacecraft may observe some key signatures of reconnection in the tail; however, that is not proof that reconnection actually occurs because other processes could

produce indistinguishable signatures. This is the essence of current debates about the nature of substorms [45,53,6,5]. On the other hand, a simulation alone, showing reconnection, proves nothing because the simulation may simply be wrong for a variety of reasons, for example bad input data, lack of resolution, too much dissipation, or missing physics. A typical example is the question of whether or not the magnetotail closes during extended periods of northward IMF [62,30,63]. Here, different models give different answers, and only a study that includes both simulations and data can be convincing. Furthermore, it is essential to test the limits of any given model, and the only possible ground truth are the observations. Global models distinguish themselves here from local models because they are actually testable by running them with measured input data and comparing the results with *in situ* observations. Local models, on the other hand, are virtually not testable because the boundary conditions are not precisely known.

That said, we compare two simulations – run with measured solar wind input – and compare the results with data. These two simulations address key issues in magnetospheric research: substorms and storms.

4.1 Substorms

The substorm of November 24, 1996, with onset at ∼2230 UT was chosen as a "GEM challenge" event because it was a typical isolated substorm following an extended period of magnetospheric quiet [67].

Figure 7a shows the IMF and solar wind data for the period of interest. After an extended period of northward IMF the IMF turns southward at around 2100 UT. Over the following 90 minutes the substorm growth phase commences until the expansion phase onset occurs around 2230 UT. It is not clear from the data (see below) whether the onset is triggered by the IMF northward turn [51] around this time; the simulation shown here indicates that this is not the case.

Figure 7b shows ground magnetometer data from the IMAGE chain compared with results from the simulation. The simulation captures the essence of the onset; however, the growth phase electrojets are stronger in the simulation, the onset is weaker, and the expansion phase is shorter.

Figure 8A compares, among other things, the polar cap magnetic flux from the simulation with estimates from Polar VIS data. Both the simulation and the data show an increase during the growth phase; however, the data indicate a larger saturation value. The beginning of the decrease coincides roughly with the expansion phase onset.

Figure 8B compares the IMP-8 magnetic field observations from the middle tail (around (-36,-3,10) R_E in the northern lobe) with the simulation results. The lobe magnetic field is a good indicator for flux and energy storage in the tail. Although the results agree qualitatively, there are significant quantitative differences. First, the loading is delayed in the simulation, and second, it is weaker than in the observed values. This indicates that there are (despite other correlations that look good) still significant discrepancies in the tail dynamics during the growth phase, similar to the ones observed in the growth phase electrojets. On the other hand, the unloading looks strikingly similar, except for a small time delay in the simulation.

Figure 9a shows the comparison with Geotail data. Geotail was also located in the middle tail ((-25,-8,-3) R_E in GSE coordinates) but close to, or in the plasma sheet. Since, whenever a spacecraft is close to a discontinuity or a sharp gradient, even a small displacement of the spacecraft can cause large changes in the observed values, we bracket the observations by taking time series from the simulation at $\pm 2R_E$ from Geotail's actual position to take this effect into account. Clearly, the simulation shows key observations, such as the earthward-tailward reversal of the flow and the sign reversal of B_z at substorm onset, the pressure and temperature peaks around onset, and the density dropout just after onset. The simulation results are often not more different from the observations than the differences in the measurements from the two plasma analyzers.

Figure 9b shows how the substorm evolution depends on parameters in the model. Specifically, we have varied the electron precipitation parameters (affecting the ionospheric conductances) and parameters in the anomalous resistivity calculation. Clearly, the substorm evolution is very sensitive to these parameters. Only for specific combinations does a substorm develop. If the parameters are such that no substorm develops the magnetosphere enters into an enhanced convection mode during which very little energy is stored in the tail, but instead the energy is dissipated by enhanced reconnection in the mid tail. It is at this point not clear whether there is a universal set of parameters that would cause a substorm every time a substorm should occur. Thus, the parameter dependence is somewhat frustrating because it limits the model's predictive capabilities. On the flip side, however, it offers the opportunity to learn more about the substorm physics. Clearly, a certain amount of ionospheric field line tying is required to let a substorm occur. At the same time, intrinsic properties of the tail are also controlling factors, in particular the onset of dissipation. Many more detailed case studies and theoretical investigation will be necessary to firmly establish these relationships. Note, that these results are not in contradiction with results from the recent "GEM reconnection challenge" [11,12,36,52,75,57], because we use a strongly nonlinear anomalous resistivity term and tail reconnection is indeed fast. Of course, the results from the "GEM reconnection challenge" offer new approaches to modeling the anomalous diffusion terms which will be pursued in the future.

The comparison of the results with data and the finding that the simulation captures the essence of the substorm development allows further investigation of the processes in the tail that go beyond the view of *in situ* spacecraft observations. Figure 10 shows 2d cuts in a plane at Z_{GSE}=-3.3 R_E which lies approximately in the center of the plasma sheet at 4 different times for the B_z component of the magnetic field, the V_x component of the velocity, and the plasma temperature. This figure demonstrates that the middle tail, where the energy conversion occurs, is highly structured. Unlike shown in many cartoons

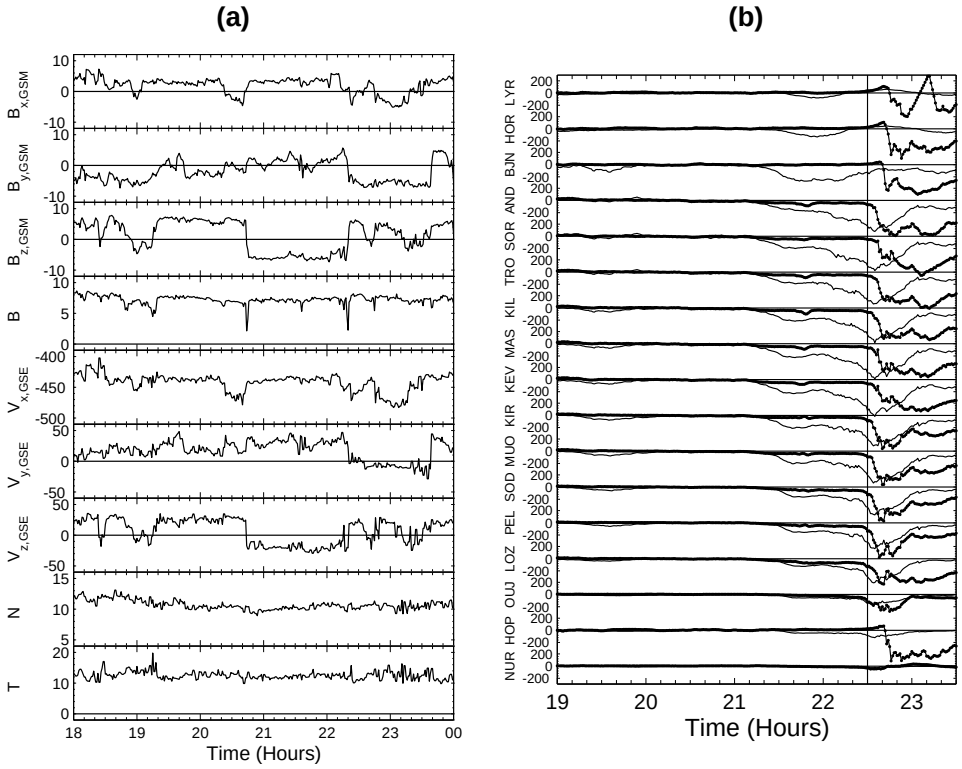

Fig. 7. **(a)** Wind interplanetary magnetic field (IMF) and solar wind data from (73,-18,8) R_E GSE on November 24, 1996. From top to bottom: the magnetic field components B_x, B_y, and B_z; the total magnetic field (all in nT, GSE); the flow velocity components V_x, V_y, and V_z (in km s^{-1}, GSE); the number density (in cm^{-3}); and the temperature (in eV). **(b)** Ground magnetometer traces from the International Monitor for Auroral Geomagnetic Effects (IMAGE) magnetometer chain on November 24, 1996 (thick dotted lines), and the comparison with the model result (thin solid line). Shown is the north-south (X) component in units of nT. The stations are Longyearbyen (LYR), Hornsund (HOR), Bear Island (BJN), Andenes (AND), Sørøya (SOR), Tromsø (TRO), Kilpisjärvi (KIL), Masi (MAS), Kevo (KEV), Kiruna (KIR), Muonio (MUO), Sodankylä (SOD), Pello (PEL), Lovozero (LOZ), Oulujärvi (OUJ), Hopen Island (HOP), Nurmijärvi (NUR)

of tail reconnection, there is more than one x-line, the existing x-lines are not simply oriented in the y-direction, and the reconnection rate varies along any given x-line. Comparing B_z with V_x shows that channels of earthward flows transport flux earthward and lead to the dipolarization of the near-Earth field, however, in a strongly local time dependent manner. The simulation even captures the phenomenon of substorm particle injection. The plasma temperature near geosynchronous orbit rises significantly at substorm expansion onset. This shows that "particle injection" is, for the most part, earthward transport and adiabatic heating of plasma, because nothing more is included in the MHD description. Of course, kinetic features, like energy dispersion, are beyond the MHD description.

We should reiterate the fact that the value of this study lies in the combination of simulation with data analysis. The simulation itself would be hardly convincing, in particular, because it depends on the correct choice of parameters. On the other hand, the data itself are too sparse and allow for many different interpretations. Taken together, however, a clearer picture emerges that lends strong support to the near-Earth neutral line model of substorms with some modifications, such as fragmented x-lines and flow channels. This does not quite solve the "substorm problem" yet, because substorms come in many different flavors and because the simulation cannot yet capture all of the details, for example auroral arcs. However, with studies like these more progress can be made.

The simulation also shows why data analysis has not yet provided a clear picture (not even a penomenological one) of the substorm process and why intelligent people might come to quite different conclusions by looking at essentially the same data sets. Figures 9a and 10 show that even a small variation in Geotail's position leads to significantly different observations. One might be tempted to conclude that studies using observations from a single (or a few) spacecraft are doomed to fail to solve the problem because they can never derive suitable synoptic maps and at best murky statistics. Thus, a convincing solution may only be found with constellations of 10's to 100's of spacecraft, along with modeling and data assimilation [2,64]. More details about this substorm and the simulation can be found in [67,68].

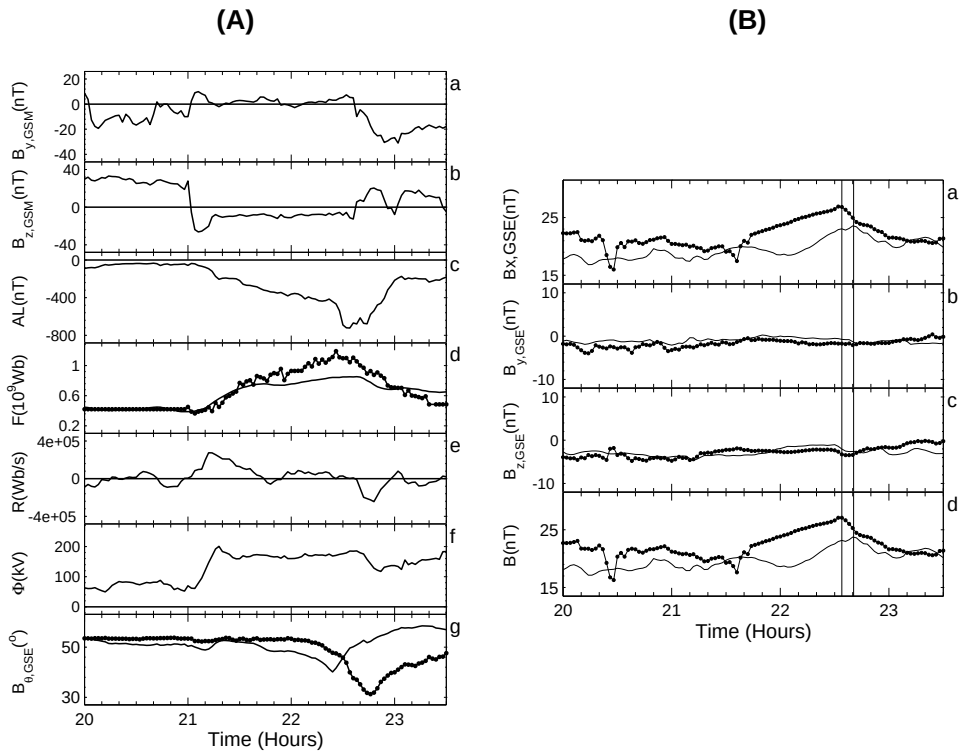

Fig. 8. (A) (a,b) Time series of the magnetic field B_y and B_z components in the magnetosheath at the subsolar magnetopause, (c) the modeled AL index, (d) the polar cap magnetic flux from the model (solid line) and from Polar Visible Imaging System (VIS) estimates (dotted line), (e) the rate of change of the polar cap flux as estimated from the model, (f) the cross polar cap potential from the model, and (g) the magnetic field elevation angle at GOES 8 from the model (solid line) and from GOES 8 (dotted line). **(B)** IMP 8 magnetic field data (dotted lines) and model results (solid lines) on November 24, 1996. GSE coordinates: (a) B_x, (b) B_y, (c) B_z, and (d) the total field. The two vertical lines mark the onset of the tail field reduction in the data and in the model, respectively

4.2 Geomagnetic storms

While substorms are manifestations of geomagnetic activity that is caused by relatively brief periods ($\sim$1h) of southward IMF, storms are caused by much longer (several hours to days) and stronger (negative IMF B_z of several 10's of nT) periods of southward IMF. In addition, the southward IMF of storms is often accompanied by high solar wind speed (sometimes over 1000 km s^{-1}) and high solar wind plasma density (several 10's cm^{-3}). Thus, storms exert much more stress on the magnetosphere and thus on any model as well. Storms are not only interesting because they cause extreme magnetospheric conditions, but also because they can cause severe space weather effects that are potentially harmful to our societal infrastructure (foremost geosynchronous and LEO satellites, power grids, and pipelines). Thus, the ability to forecast storm effects has recently become a topic of strong interest. Of course, global modeling in an operational setting would be one key element of space weather forecasting.

In the following we present a comparison of our model predictions with several key data sets for the Bastille Day storm (July 14/15, 2000), which was one of the strongest storms so far of this solar cycle [71]. We concentrate on space weather effects, that is, magnetospheric compression and ground magnetic perturbations.

Figure 11 shows the solar wind and IMF parameters for this event. The main characteristics are an interplanetary shock at $\sim$1430 UT, followed by the CME sheath until $\sim$1920 UT, followed by the CME proper, which lasts for almost 1 day. The solar wind speed reaches values of $\sim$1100 km s^{-1}, the density 20 cm^{-3}, and the IMF B_z -60 nT (at $\sim$2000 UT, the peak of the storm.)

Figure 12 shows the comparison of the magnetic field B_z component with measurements from three GOES geosynchronous satellites. First, compared to a typical quiet day (July 13, 2000), the field at these satellites is extremely distorted. In particular, the field measurements show several episodes in which B_z becomes negative, indicating that the spacecraft have crossed the magnetopause and entered the magnetosheath or even the solar wind. The simulation results compare extremely well with the observations, predicting all but a few of the magnetopause crossings.

Figure 13 shows the extreme compression and distortion of the magnetosphere at the peak of the storm. The magnetopause

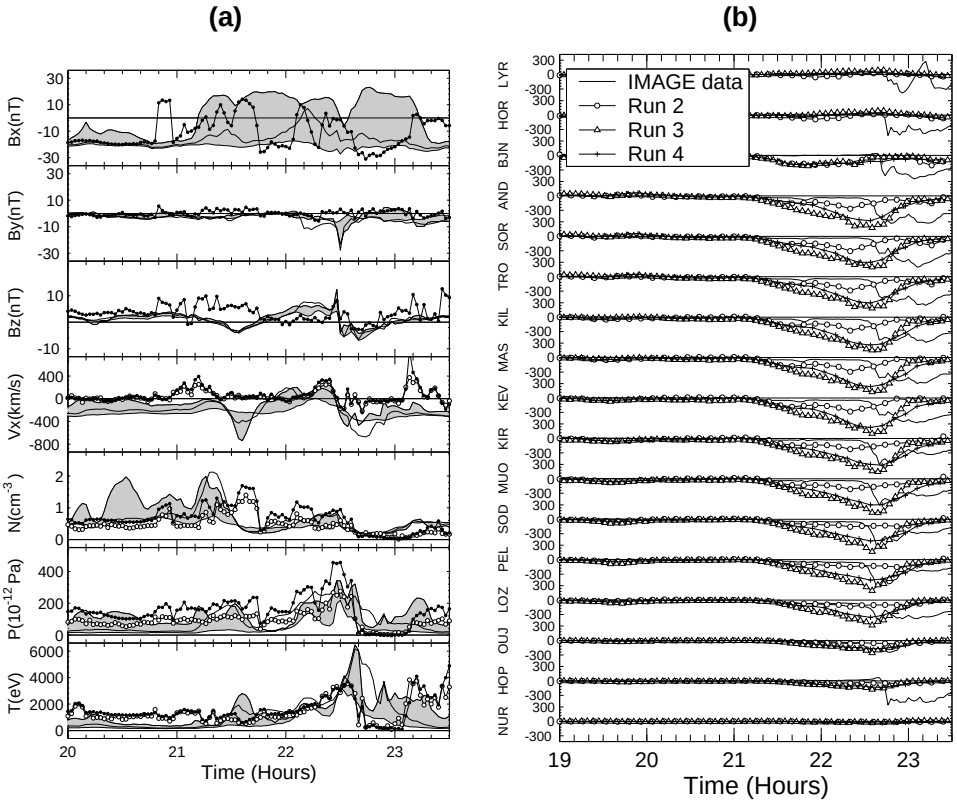

Fig. 9. (a) Geotail magnetic field and plasma data and comparison with the model results, on November 24, 1996. The dotted lines are magnetic field and plasma data from the Magnetic Field Experiment (MGF) and Low Energy Particle (LEP) experiment, respectively. Data represented with open circles are from the Comprehensive Plasma Instrumentation (CPI) instrument. Model results at the nominal Geotail position are drawn with a heavy solid line. The shaded area is bounded by time series taken from the model at locations that are 2 R_E above and below Geotail, respectively. **(b)** Comparison of IMAGE ground magnetometer recordings on November 24, 1996, with the results from three different simulation runs that did not produce a substorm (see text for details). The format of this figure is the same as that of Fig. 7b

comes at this time as close as 4.9 R_E to Earth. At this time the dynamic pressure of the solar wind is 12 times as large as its average value, and the IMF B_z value is nearly -60 nT. The former causes a compression of the magnetosphere, while the latter causes flux erosion. Neither of these effects alone could bring the magnetopause this far in, but the combined effect does. Because storm effects of this magnitude are extremely rare (at most a few per solar cycle) events like this one put empirical models out of their valid parameter range, thus prediction is more reliable with numerical models.

The peculiar shape of the dayside magnetosphere has also consequences for the cross polar cap potential (CPCP). Simple prediction of the CPCP by regression formulas [72,44] yield CPCP values of the order of 1000 kV. However, the model and measurements show that the CPCP reaches only $\sim$300 kV, thus, the CPCP saturates at this level. Figure 13 indicates indicates that because of the strong magnetopause erosion flux piles up in the lobes and the lobe shoulders bulge out. This causes the reconnection region to be partially shielded from the solar wind and the compressed IMF in the magnetosheath. Because of this shielding less magnetic energy can be transported to the reconnection site, leading to an overall reduction in the reconnection rate, and thus magnetospheric and ionospheric convection.

Figure 14 shows the comparison of ground magnetometer recordings with predictions from the simulation. The quality of the prediction varies significantly from station to station but is generally better at high and sub-auroral latitudes, and worst in the nightside auroral zone. Comparing the fluctuations, i.e., the time derivative of the magnetic field (which are the cause of induced electric fields in power lines or pipelines) shows a similar picture. Figure 15 combines the spectral power of about 40 ground magnetometers in different latitude zones. Except for the auroral zone, the predictions of the power spectrum of the fluctuations is surprisingly good in the 0-3 mHz range. However, as said, this is not necessarily true for individual stations. In other words, the model predictions of the total power flux are more or less accurate; however, the model cannot yet predict the correct locations of large wave power flux. This event is discussed in more detail in [71].

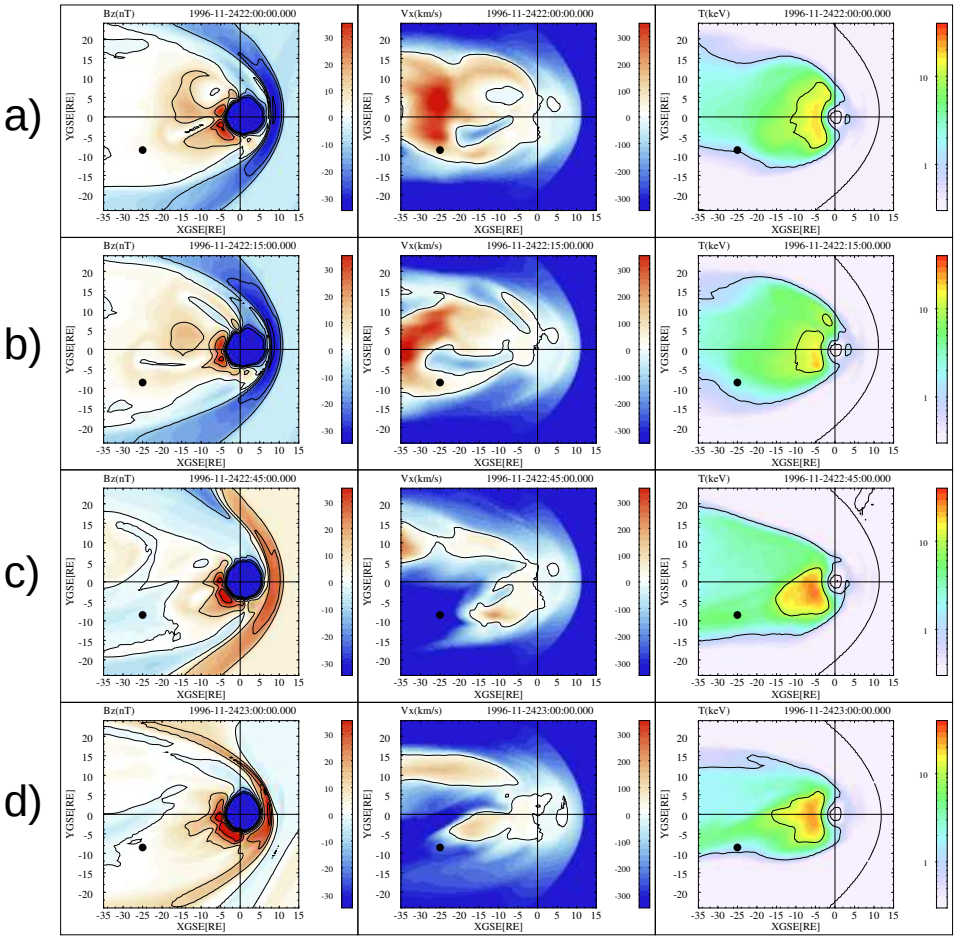

Fig. 10. The magnetic field B_z component, the velocity V_x component, and the plasma temperature in a plane at Z_{GSE}=-3.3 R_E, at four different times: (a) 2200 UT, (b) 2215 UT, (c) 2245 UT, and (d) 2300 UT. Contours are drawn at the zero level for V_x, at 12 nT intervals for B_z, and at 1 and 10 keV for the temperature, respectively. The black dot marks Geotail's position.

4.3 Lessons from data comparisons

In the preceding sections we have shown that our model can reproduce a number of characteristic phenomena of substorms and storms. In particular, the model shows the magnetic energy loading in the tail during the substorm growth phase, the dipolarization of the near-Earth magnetic field in the expansion phase, the concurrent injection of energetic plasma into the inner magnetosphere, the formation of new x-lines, the formation and ejection of a plasmoid, and the intensification of the westward electrojet at expansion phase onset. Although these phenomena have all been observed in the past, no comprehensive (and universally accepted) model exists yet that puts these phenomena into context and provides a satisfactory explanation. The fact that our model produces these phenomena, *and* the fact that these are all related to the onset of reconnection in the near-Earth tail at $\sim$20 R_E lends support to the Near Earth Neutral Line (NENL) model [53,6]. However, we also find that the tail dynamics is much more complex compared to the NENL prediction. In particular, the substorm onset is characterized by multiple x-lines that form at different local times and distances, and which produce rapid earthward and tailward plasma flows akin to Bursty Bulk Flows (BBFs) [1,4,3]. This fragmentation of the tail plasma sheet makes it all but impossible to solve the "2 minute problem," that is, the exact onset location and cause of the substorm expansion phase onset. We should also not forget that the model can not at present produce the brightening of the equator most auroral arc at onset, which is often cited as the first distinct substorm signature [47,46,27].

As far as magnetic storms are concerned, the study presented here should be viewed as a first step to model the magnetosphere under extreme solar wind conditions. This aspect is not only of particular importance for space weather, but also shows that the magnetosphere can exhibit a very particular behavior during storms. For example, both the simulation and the data show that the polar cap potential saturates when the driving solar wind ingredient, that is, the interplanetary electric field E_{ip}, reaches very high ($>\sim$20 mV/m) values. For more benign conditions there is a more or less linear relationship between

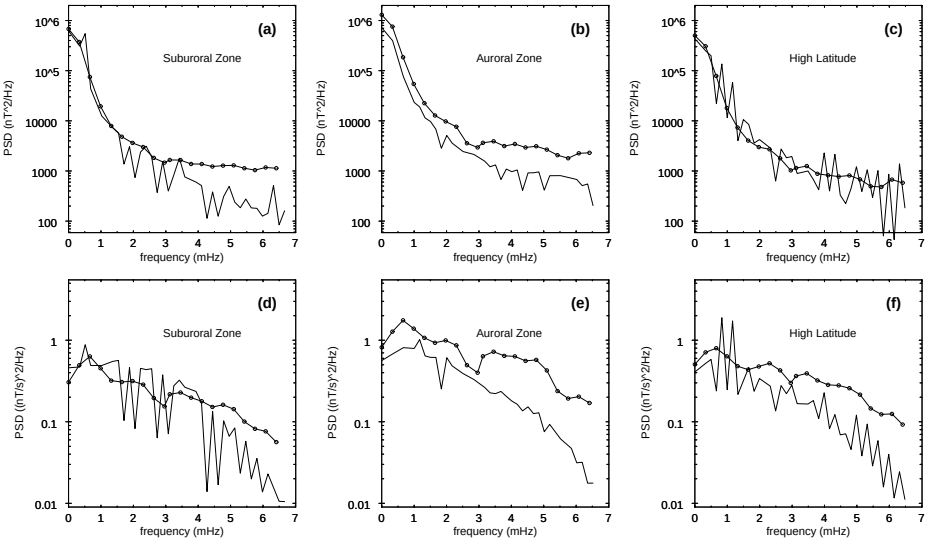

Fig. 15. (a-c) shows the averaged power spectral density (PSD, in units of nT^2Hz^{-1}) of the north-south perturbation for ground magnetometer stations in the sub-auroral zone (a), the auroral zone (b), and the polar cap (c). The solid line is for the data, the solid line with dots represents the model result. The lower panel (d-f) shows the average PSD of the time derivative of the north-south perturbation (in units of $nT^2s^{-2}Hz^{-1}$) for the same set of stations

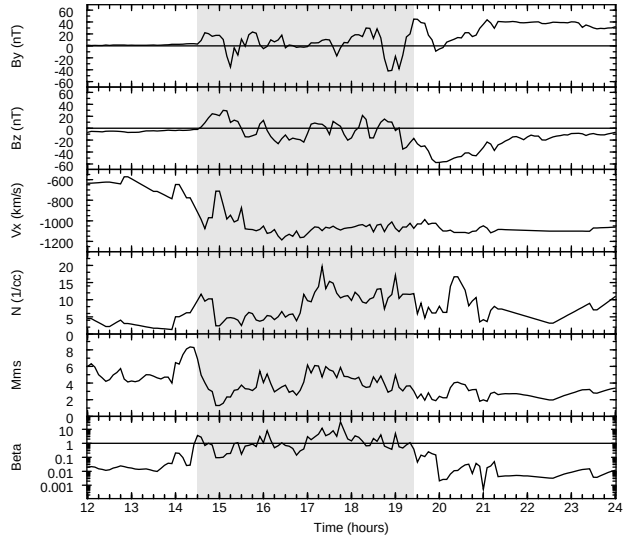

Fig. 11. Solar wind and IMF measurements for July 15, 2000. From top to bottom: The IMF B_y and B_z components, the solar wind velocity, the solar wind number density, the solar wind magnetosonic Mach number, and the plasma β (ratio of plasma pressure to magnetic field pressure). The shaded region is the CME sheath, which begins at the interplanetary shock and ends with the CME proper, which is defined here as the magnetic flux rope

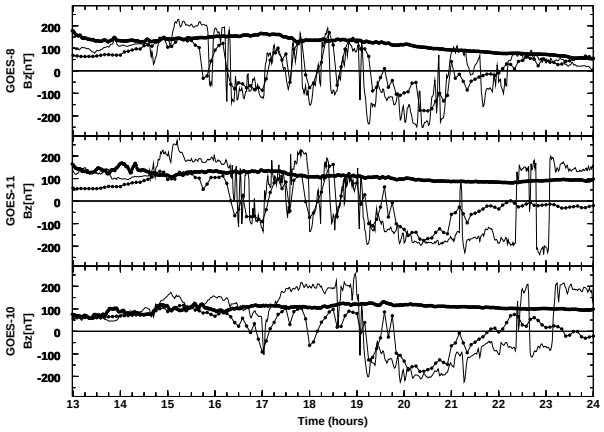

Fig. 12. The magnetic field component B_z observed by the 3 GOES satellites (from top to bottom: GOES 8, GOES 11, and GOES 10, ordered in increasing east longitude). The GOES data on July 15, 2000 are plotted as black solid lines, the corresponding model results as black lines with dots, and the GOES data for July 13, 2000 are plotted as thick black line. The latter data are from a typical geomagnetically quiet day

E_{ip} and the potential [72,15] which apparently loses its validity for the strong solar wind driving during storms. This result leads to a host of other questions, for example, if similar nonlinearities also exist for the energy input and dissipation in the magnetosphere. Global models face here a severe limitation because the most characteristic signature of a geomagnetic storm is the ring current which can not be treated adequately. Ring current formation is caused by the trapping of energetic plasma ($>\sim$10 keV ions) in the inner part (2.5 – 8 R_E) of the magnetosphere by gradient and curvature drifts. The MHD formalism does not include these drifts; they are, in fact a consequence of non-Maxwellian distributions [34,35]. Thus, until global mod-

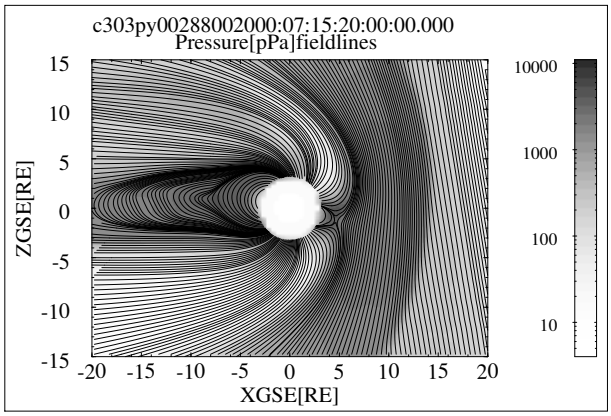

Fig. 13. Cut of the noon-midnight meridional plane shows the plasma pressure in grayscale and magnetic field lines at 2000 UT on July 15, 2000

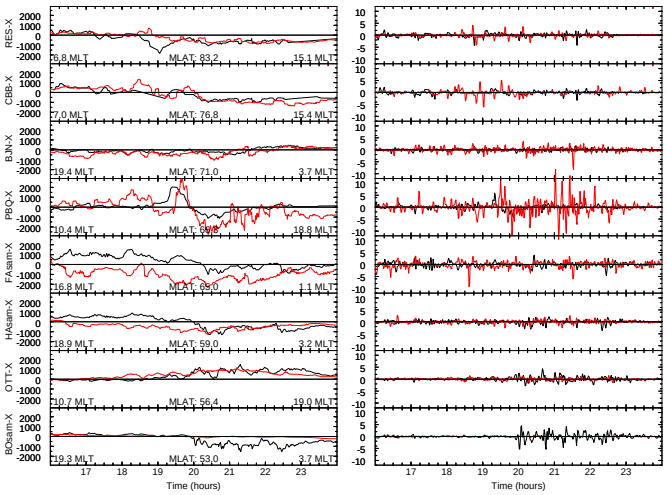

Fig. 14. The north-south ground magnetic perturbation (left column, the scale is in nT) and the corresponding time derivative (right column, the scale is in nT/s) for 8 ground magnetometer stations. The station names are indicated at the left of each panel, and the stations are ordered from north to south, although at different magnetic local times. Specifically, these stations are, with their abbreviation, geographic longitude and latitude given in parentheses: Resolute Bay (RES, 74.7°, 265.2°), Cambridge Bay (CBB, 69.1°, 255.0°), Bear Island (BJN, 74.52°, 19.02°), Poste-d.l.-Baleine (PBQ, 55.3°, 282.3°), Faroes (FAsam, 62.1°, 353.0°), Hankasalmi (HAsam, 62.3°, 26.7°), Ottawa (OTT, 45.4°, 284.5°), and Borok (BOsam, 58.0°, 38.3°). The black lines show the data and the red lines show the simulation results.

els are coupled with appropriate models of the inner magnetosphere (see below) such studies will be difficult.

5 Future directions

The development of global geospace models has by no means come to an end. There are a large number of regions and processes that are not currently covered or that need improvement. At present some model developments appear most promising:

- The inclusion of the particle drift physics in the inner magnetosphere in the form of sub-models similar to the Rice Convection Model (RCM).
- Adaptive grid solvers that allow better resolution of plasma and field boundaries along with reduced numerical diffusion.
- Better magnetosphere-ionosphere coupling, in particular a more self-consistent model for electron precipitation.
- A multi-fluid formalism to study the ionospheric outflow and the role of ionospheric plasma in the magnetosphere. This includes the need for an outflow specification model or a self-consistent outflow model, none of which exists yet.
- Data assimilation from multiple spacecraft observations.

6 Conclusions

Global modeling has been proven an extremely powerful tool to study the solar-terrestrial plasma interaction. It's importance will likely increase in the future as models become ever more sophisticated and as computational power becomes ever more abundant and cheaper. We are now entering an era where global modeling does no longer depend on expensive supercomputers, but where affordable desktop equipment (Beowulf PC clusters) is becoming sufficient for meaningful global modeling. This should foster the more widespread use of global models, not only by the model developers themselves, but also by others in the scientific community.

7 Acknowledgements

This work was supported by grants ATM-0097143 and ATM-0084483 from the National Science Foundation and by grants NAG 5-10986 and NAG 5-12107 from the National Aeronautics and Space Administration.

References

1. V. Angelopoulos, W. Baumjohann, C. F. Kennel, F. V. Coroniti, M. G. Kivelson, R. Pellat, R. J. Walker, H. Lühr, and G. Paschmann. Bursty bulk flows in the inner plasma sheet. *J. Geophys. Res.*, 97:4027, 1992.
2. V. Angelopoulos, C. W. Carlson, D. W. Curtis, P. Harvey, R. P. Lin, F. S. Mozer, D. H. Pankow, J. Raeder, and C. T. Russell. On the necessity and feasability of a equatorial magnetospheric constellation. In V. Angelopoulos and P. V. Panetta, editors, *Science Closure and Enabling Technologies for Constellation Class Missions*, page 14. University of California, Berkeley, and NASA Goddard Space Flight Center, 1998.
3. V. Angelopoulos, C. F. Kennel, F. V. Coroniti, R. Pellat, M. G. Kivelson, R. J. Walker, C. T. Russell, W. Baumjohann, W. C. Feldman, and J. T. Gosling. Statistical chracteristics of bursty bulk flow events. *J. Geophys. Res.*, 99:21257, 1994.

4. V. Angelopoulos, Baumjohann W, C. F. Kennel, F. V. Coroniti, M. G. Kivelson, R. Pellat, R. J. Walker, H. Luhr, and G. Paschmann. Bursty bulk flows in the inner central plasma sheet. *J. Geophys. Res.*, 97:4027, 1992.
5. D. N. Baker, A. J. Klimas, D. Vassiliadis, T. I. Pulkkinen, and R. L. McPherron. Reexamination of driven and unloading aspects of magnetospheric substorms. *J. Geophys. Res.*, 102:7169, 1997.
6. D. N. Baker, T. I. Pulkkinen, V. Angelopoulos, W. Baumjohann, and R. L. McPherron. Neutral line model of substorms: Past results and present view. *J. Geophys. Res.*, 101:12975, 1996.
7. D. S. Balsara and D. Spicer. Maintaining pressure positivity in magnetohydrodynamic simulations. *J. Comp. Phys.*, 148:133, 1999.
8. A. R. Barakat and R. W. Schunk. Transport equations for multicomponent anisotropic space plasmas: A review. *Plasma Phys.*, 24:389, 1982.
9. M. J. Berger and P. Colella. Local adaptive mesh refinement for shock hydrodynamics. *J. Comp. Phys.*, 82:64, 1989.
10. M. J. Berger and J. Olinger. Adaptive mesh refinement for hyperbolic partial differential equations. *J. Comp. Phys.*, 53:484, 1984.
11. J. Birn, J. F. Drake, M. A. Shay, B. N. Rogers, R. E. Denton, M. Hesse, M. Kuznetsova, Z. W. Ma, A. Bhattacharjee, A. Otto, and P. L. Pritchett. Geospace Environmental Modeling (GEM) magnetic reconnection challenge. *J. Geophys. Res.*, 106:3715, 2001.
12. J. Birn and M. Hesse. Geospace Environmnent Modeling (GEM) magnetic reconnection challenge: resistive tearing, anisotropic pressure and hall effects. *J. Geophys. Res.*, 106:3737, 2001.
13. J. P. Boris. A physically motivated soluton of the Alfvèn problem, *nrl memorandum report 2167*, Naval Research Laboratory, Washington, D.C., 1970.
14. J. P. Boris and D. L. Book. Flux corrected transport: I. SHASTA, a fluid transport algorithm that works. *J. Comp. Phys.*, 11:38, 1973.
15. C. B. Boyle, P. H. Reiff, and M. R. Hairston. Empirical polar cap potentials. *J. Geophys. Res.*, 102:111, 1997.
16. J. U. Brackbill and D. C. Barnes. The effect of nonzero div B on the numerical solution of the magnetohydrodynamic equations. *J. Comp. Phys.*, 35:426, 1980.
17. S. H. Brecht. Global simulations using MHD codes: A few points to consider before you try one. *Space Sci. Rev.*, 42:169, 1985.
18. S. H. Brecht, J. G. Lyon, J. A. Fedder, and K. Hain. A time dependent three dimensional simulation of the Earth's magnetosphere: Reconnection events. *J. Geophys. Res.*, 87:6098, 1982.
19. M. Brio and C. C. Wu. An upwind differencing scheme for the equations of ideal magnetohydrodynamics. *J. Comp. Phys.*, 75:400, 1988.
20. W. Dai and P. R. Woodward. A high-order Godunov-type scheme for shock interactions in ideal magnetohydrodynamics. *SIAM J. Sci. Comp.*, 18:957, 1997.
21. C. R. DeVore. Flux-corrected transport techniques for multidimensional compressible magnetohydrodynamics. *Journal of Computational Physics*, 92:142, 1991.
22. C. R. Evans and J. F. Hawley. Simulation of magnetohydrodynamic flows: A constrained transport method. *Astrophys. J.*, 332:659, 1988.
23. J. A. Fedder and J. G. Lyon. The solar wind - magnetosphere - ionosphere current - voltage relationship. *Geophys. Res. Lett.*, 14:880, 1987.
24. J. A. Fedder, S. P. Slinker, and J. G. Lyon. A comparison of global numerical simulation results to data for the January 27-28, 1992, geospace environment modeling challenge event. *J. Geophys. Res.*, 103:14799, 1998.
25. J. A. Fedder, S. P. Slinker, J. G. Lyon, and R. D. Elphinstone. Global numerical simulation of the growth phase and the expansion onset for a substorm observed by Viking. *J. Geophys. Res.*, 100:19083, 1995.
26. L. A. Frank, M. Ashour-Abdalla, J. Berchem, J. Raeder, W. R. Paterson, S. Kokubun, T. Yamamoto, R. P. Lepping, F. V. Coroniti, D. H. Fairfield, and K. L. Ackerson. Observations of plasmas and magnetic fields in Earth's distant magnetotail: Comparison with a global MHD model. *J. Geophys. Res.*, 100:19177, 1995.
27. L. A. Frank, W. R. Paterson, J. B. Sigwarth, and T. Mukai. Observations of plasma sheet dynamics earthward of the onset region with the Geotail spacecraft. *J. Geophys. Res.*, 106:18823, 2001.
28. T. J. Fuller-Rowell, D. Rees, S. Quegan, R. J. Moffett, M. V. Codrescu, and G. H. Millward. A coupled thermosphere-ionosphere model (CTIM). In R. W. Schunk, editor, *STEP Report*, page 217, NOAA/NGDC, Boulder, Colorado, 1996. Scientific Committee on Solar Terrestrial Physics (SCOSTEP).
29. T. I. Gombosi. ????????????? *this book*, ???????:???????, 2002.
30. T. I. Gombosi, K. G. Powell, and B. van Leer. Comment on "Modeling the magnetosphere for northward interplanetary magnetic field: Effects of numerical resistivity" by Joachim Raeder. *J. Geophys. Res.*, 105:13141, 2000.
31. A. Harten. On a class of high resolution total variation stable finite difference schemes. *SIAM J. Num. Anal.*, 21:1, 1984.
32. A. Harten, A. Hyman, and P. D. Lax. On finite difference approximations and entropy conditions for shocks. *Comm. Pure and Appl. Math.*, 29:297, 1976.
33. A. Harten and G. Zwas. Self-adjusting hybrid schemes for shock computations. *J. Comput. Phys.*, 9:568, 1972.
34. M. Heinemann. Role of collisionless heat flux in magnetospheric convection. *J. Geophys. Res.*, 104:28397, 1999.
35. M. Heinemann and R. A. Wolf. Relationships of models of the inner magnetosphere to the Rice Convection Model. *J. Geophys. Res.*, 106:15545, 2001.
36. M. Hesse, J. Birn, and M. Kuznetsova. Collisionless magnetic reconnection: electron process and transport modeling. *J. Geophys. Res.*, 106:3721, 2001.
37. C. Hirsch. *Numerical Computation of Internal and External Flow*, volume II. John Wiley, New York, 1990.
38. P. Janhunen, T. I. Pulkkinen, and K. Kauristie. Auroral fading in ionosphere-magnetosphere coupling model: Implications for possible mechanisms. *Geophys. Res. Lett.*, 22:2049, 1995.
39. G.-S. Jiang and C. C. Wu. A high-order WENO finite difference scheme for the equations of idel magnetohydrodynamics. *J. Comp. Phys.*, 150:561, 1999.
40. S. Knight. Parallel electric fields. *Planet. Space Sci.*, 21:741, 1972.
41. P. D. Lax and B. Wendroff. Systems of conservation laws. *Comm. Pure Appl. Math.*, 13:217, 1960.
42. J. N. Leboeuf, T. Tajima, C. F. Kennel, and J. M. Dawson. Global simulation of the time dependent magnetosphere. *Geophys. Res. Lett.*, 5:609, 1978.
43. X. Liu, S. Osher, and T. Chan. Weighted essentially nonoscillatory schemes. *J. Comp. Phys.*, 115:200, 1994.
44. G. Lu, P. H. Reiff, M. R. Hairston, R. A. Heelis, and J. L. Karty. Distribution of convection potential around the polar cap boundary as a function of the interplanetary magnetic field. *J. Geophys. Res.*, 94:13447, 1989.
45. A. T. Y. Lui. Extended consideration of a synthesis model for magnetic substorms. In J. R. Kan, T. A. Potemra, S. Kokubun, and T. Ijima, editors, *Magnetospheric Substorms*, volume 64, page 43. AGU Monogr. Ser., American Geophysical Union, 1991.
46. A. T. Y. Lui, R. E. Lopez, B. J. Anderson, K. Takahashi, L. J. Zanetti, R. W. McEntire, T. A. Potemra, D. M. Klumpar, greene, and strangeway. Current disruptions in the near-Earth neutral sheet region. *J. Geophys. Res.*, 97:1461, 1992.
47. A. T. Y. Lui, R. E. Lopez, S. M. Krimigis, R. W. McEntire, L. J. Zanetti, and T. A. Potemra. A case study of magnetotail current sheet disruption and diversion. *Geophys. Res. Lett.*, 15:721, 1988.
48. J. G. Lyon, S. H. Brecht, J. A. Fedder, and P. J. Palmadesso. Computer simulation of a geomagnetic substorm. *Phys. Rev. Lett.*, 46:1038, 1981.
49. J. G. Lyon, R. E. Lopez, C. C. Goodrich, M. Wiltberger, and K. Papadopoulos. Simulation of the March 9, 1995, substorm: Auroral brightening and the onset of lobe reconnection. *Geophys. Res. Lett.*, 25:3039, 1998.
50. L. R. Lyons. The Geospace Environment Modeling Grand Challenge. *J. Geophys. Res.*, 103:14781, 1998.

51. L. R. Lyons, R. L. McPherron, E. Zesta, G. D. Reeves, J. B. Sigwarth, and L.A. Frank. Timing of substorm signatures during the November 24, 1996 geospace environment modeling event. *J. Geophys. Res.*, submitted, 2000.
52. Z. W. Ma and A. Bhattacharjee. Hall magnetohydrodynamic reconnection: the geospace environment modeling challenge. *J. Geophys. Res.*, 106:3773, 2001.
53. R. L. McPherron. Physical processes producing magnetospheric substorms and magnetic storms. In J. Jacobs, editor, *Geomagnetism*, volume 4, page 593. Academic Press, 1991.
54. J. Moen and A. Brekke. The solar flux influence on quiet time conductances in the auroral ionosphere. *Geophys. Res. Lett.*, 20:971, 1993.
55. T. Ogino. A three dimensional MHD simulation of the interaction of the solar wind with the Earth's magnetosphere: The generation of field aligned currents. *J. Geophys. Res.*, 91:6791, 1986.
56. T. Ogino, R. J. Walker, and M. Ashour-Abdalla. A global magnetohydrodynamic simulation of the response of of the magnetosphere to a northward turning of the interplanetary magnetic field. *J. Geophys. Res.*, 99:11027, 1994.
57. A. Otto. Geospace environment modeling (GEM) magnetic reconnection challenge: MHD and Hall MHD – constant and current dependent resistivity models. *J. Geophys. Res.*, 106:3751, 2001.
58. E. N. Parker. The alternative paradigm for magnetospheric physics. *J. Geophys. Res.*, 101:10587, 1996.
59. V. Pierrard, G. V. Khazanov, and J. F. Lemaire. Current–voltage relationship. *J. Atm. Sol.-Terr. Phys.*, 69:2048, 2007.
60. K. G. Powell, P. L. Roe, T. J. Linde, T. I. Gombosi, and D. L. DeZeeuw. A solution-adaptive upwind scheme for ideal magnetohydrodynamics. *J. Comp. Phys.*, 154:284, 1999.
61. J. Raeder. Global MHD simulations of the dynamics of the magnetosphere: Weak and strong solar wind forcing. In J. R. Kan, J. D. Craven, and S.-I. Akasofu, editors, *Proceedings of the Second International Conference on Substorms*, page 561. Geophysical Institute, Univ. of Alaska Fairbanks, 1995.
62. J. Raeder. Modeling the magnetosphere for northward interplanetary magnetic field: Effects of electrical resistivity. *J. Geophys. Res.*, 104:17357, 1999.
63. J Raeder. Reply. *J. Geophys. Res.*, 105:13149, 2000.
64. J. Raeder and V. Angelopoulos. Using global simulations of the magnetosphere for multi-satellite mission planning and analysis,. In V. Angelopoulos and P. V. Panetta, editors, *Science Closure and Enabling Technologies for Constellation Class Missions*, page 78. University of California, Berkeley, and NASA Goddard Space Flight Center, 1998.
65. J. Raeder, J. Berchem, and M. Ashour-Abdalla. The importance of small scale processes in global MHD simulations: Some numerical experiments. In T. Chang and J. R. Jasperse, editors, *The Physics of Space Plasmas*, volume 14, page 403, Cambridge, Mass., 1996. MIT Cent. for Theoret. Geo/Cosmo Plasma Phys.
66. J. Raeder, J. Berchem, M. Ashour-Abdalla, L. A. Frank, W. R. Paterson, K. L. Ackerson, R. P. Lepping, S. Kokubun, T. Yamamoto, and S. A. Slavin. Boundary layer formation in the magnetotail: Geotail observations and comparisons with a global MHD model. *Geophys. Res. Lett.*, 24:951, 1997.
67. J. Raeder and N. Maynard. Foreword. *J. Geophys. Res.*, 106:345, 2001.
68. J. Raeder, R. L. McPherron, L. A. Frank, W. R. Paterson, J. B. Sigwarth, G. Lu, H. J. Singer, S. Kokubun, T. Mukai, and J. A. Slavin. Global simulation of the geospace environment modeling substorm challenge event. *J. Geophys. Res.*, 106:381, 2001.
69. J. Raeder, R. J. Walker, and M. Ashour-Abdalla. The structure of the distant geomagnetic tail during long periods of northward IMF. *Geophys. Res. Lett.*, 22:349, 1995.
70. J. Raeder, Y. Wang, and T. Fuller-Rowell. Geomagnetic storm simulation with a coupled magnetosphere - ionosphere - thermosphere model. In P. Song, G. Siscoe, and H. J. Singer, editors, *Space Weather, AGU Geophys. Monogr. Ser.*, volume 125, page 377. American Geophysical Union, 2001.
71. J. Raeder, Y. L. Wang, T. J. Fuller-Rowell, and H. J. Singer. Global simulation of space weather effects of the Bastille Day storm. *Sol. Phys.*, 204:325, 2001.
72. P. H. Reiff, R. W. Spiro, and T. W. Hill. Dependence of polar cap potential drop of interplanetary parameters. *J. Geophys. Res.*, 86:7639, 1981.
73. A. D. Richmond and R. G. Roble. Electrodynamic effects of thermospheric winds for the NCAR thermospheric general circulation model. *J. Geophys. Res.*, 92:12365, 1987.
74. R. M. Robinson, R. R. Vondrak, K. Miller, T. Dabbs, and D. Hardy. On calculating ionospheric conductances from the flux and energy of precipitating electrons. *J. Geophys. Res.*, 92:2565, 1987.
75. M. A. Shay, J. F. Drake, B. N. Rogers, and R. E. Denton. Alfvenic collisionless magnetic reconnection and the Hall term. *J. Geophys. Res.*, 106:3759, 2001.
76. G. A. Sod. *Numerical Methods in Fluid Dynamics*. Cambridge University Press, Cambridge, 1985.
77. B. U. O. Sonnerup and L. J. Cahill. Magnetopause structure and attitude from Explorer 12 observations. *J. Geophys. Res.*, 72:171, 1967.
78. B. U. O. Sonnerup and L. J. Cahill. Explorer 12 observations of the magnetopause current layer. *J. Geophys. Res.*, 73:1757, 1968.
79. R. J. Strangeway, R. C. Elphic, W. J. Peria, and C. W. Carlson. FAST observations of electromagnetic stresses applied to the polar ionosphere. volume 118, page 21. AGU Monogr. Ser., American Geophysical Union, 1999.
80. R. J. Strangeway and J. Raeder. On the transition from collisionless to collisional magnetohydrodynamics. *J. Geophys. Res.*, 106:1955, 2001.
81. P. K. Sweby. High resolution schemes using flux limiters for hyperbolic conservation laws. *SIAM J. Num. Anal.*, 21:995, 1984.
82. T. Tanaka. Generation mechanisms for magnetosphere-ionosphere current systems deduced from a three-dimensional MHD simulation of the solar wind-magnetosphere-ionosphere coupling processes. *J. Geophys. Res.*, 100:12057, 1995.
83. G. Toth. The $\nabla \cdot B$ constraint in shock-capturing magnetohydrodynamics codes. *J. Comp. Phys.*, 161:605, 2000.
84. A. Usadi, A. Kageyama, K. Watanabe, and T. Sato. A global simulation of the magnetosphere with a long tail: Southward and northward interplantary magnetic field. *J. Geophys. Res.*, 98:7503, 1993.
85. B. Van Leer. Towards the ultimate conservative difference scheme. I. The quest for monotonicity. In *Lecture Notes in Physics*, volume 18, page 163. Springer Verlag, Berlin, 1973.
86. B. Van Leer. Towards the ultimate conservative difference scheme. II. Monotonicity and conservation combined in a second order scheme. *J. Comp. Phys.*, 14:361, 1974.
87. B. Van Leer. Towards the ultimate conservative difference scheme. III. Upstream centered finite difference schemes for ideal compressible flow. *J. Comp. Phys.*, 23:263, 1977.
88. V. M. Vasyliunas. Mathematical models of magnetospheric convection and its coupling to the ionosphere. In *Particles and Fields in the Magnetosphere*, page 61. Dordrecht, Netherlands: D. Reidel, 1970.
89. K. Watanabe and T. Sato. Global simulation of the solar wind-magnetosphere interaction: The importance of its numerical validity. *J. Geophys. Res.*, 95:75, 1990.
90. R. A. Wolf. The quasi-static (slow flow) region of the magnetosphere. In R. L. Carovillano and J. M. Forbes, editors, *Solar Terrestrial Physics*, page 303. D. Reidel, Hingham, MA, 1983.
91. H. C. Yee. On symmetric and upwind TVD schemes. In *Proc. 6th GAMM Conference on Numerical Methods in Fluid Dynamics*, page 399, Braunschweig, 1985. Vieweg.
92. H. C. Yee. Construction of explicit and implicit symmetric TVD schemes and their applications. *J. Comput. Phys.*, 68:151, 1987.
93. A. L. Zachary, A Malagoli, and P. Colella. A higher-order Godunov method for multi-dimensional ideal magnetohydrodynamics. *SIAM J. Sci. Comp.*, 15:263, 1994.

94. S. T. Zalesak. Fully multidimensional flux-corrected transport. *J. Comp. Phys.*, 31:355, 1979.
95. S. T. Zalesak. Very high order pseudospectral flux-corrected transport (FCT) algorithms for conservation laws. In R. Vichnevetsky and R. S. Stepleman, editors, *Proceedings of the Fourth IMACS International Symposium on Computer Methods for Partial Differential Equations*, page 126, New Brunswick, 1981. IMACS, Rutgers University.

auroral precipitation, 9

BBF, 14
Boris correction, 4
boundary conditions, 4
bow shock, 1
Bursty Bulk Flows, 14

CFL criterion, 4
CME, 12
conductance
– Hall, 8
– ionospheric, 8
– Pedersen, 8
conservative difference schemes, 5
convection
– challenge, 1
– enhanced, 10
– ionosphere, 1
– magnetospheric, 1, 8
– potential, 7
CPCP, 13
cross polar cap potential, 13
CTIM, 8
current
– field-aligned, 1

data assimilation, 11, 16
diffusion
– anomalous, 3
dipolarization, 11
dipole field, 7
distribution function, 2
divergence-free, 7

Earth
– dipole, 3
eigenvector
– degenerate, 5
electric field, 7
electrojet, 10
electron precipitation
– diffuse, 8
– discrete, 8
ENO, 6
equations
– Boltzmann, 1
– Maxwell, 1
– non-conservative, 6
– Vlasov, 1
error terms, 6
Essentially Non-oscillatory, 6

FAC, 1, 7
Faraday's law, 6
FCT, 6
field line tying, 10
finite differences, 5
finite element method, 2, 5
finite volume method, 2, 5
flow
– supermagnetosonic, 1
flux conservation, 6
– magnetic, 6
Flux Corrected Transport, 6
flux hybridization, 6
Flux Limiter, 6

GEM
– reconnection challenge, 10
geospace, 1
Geotail, 10
global conservation, 5
global magnetosphere model, 9
GOES, 12
grid
– Cartesian, 2
– hierarchy, 2
– non-Cartesian, 2
– numerical, 1
– staggered, 6
– stretched Cartesian, 2, 7
– unstructured, 2
ground magnetic perturbations, 12
ground magnetometer, 10, 13

Harten's Lemma, 6
hmF2, 9
hybridization, 6

IMF, 9, 10
IMP-8, 10
initial conditions, 4
ionosphere, 1, 7, 8
ionospheric outflow, 16
ISTP, 1

Knight relation, 8

LFM, 2
load balancing, 2
Lyon-Fedder-Mobarry, 2

Mach number
– magnetosonic, 1
magnetic field, 7
magnetic flux, 7
magnetic reconnection, 3
magnetohydrodynamic, 1, 2

Index

magnetopause, 1, 12
magnetosheath, 12
magnetosphere, 1, 9
– compression, 13
mapping, 7
Maxwell equation, 6
Maxwellian distribution, 2
MHD, 1, 2
– conservative, 3
– non-conservative, 3
– normalization, 3
– semi-conservative, 3
model
– geospace, 1
– global, 1
– magnetosphere, 1
– multi-fluid, 8
– near-Earth neutral line, 11
Modeling
– geospace, 1
modeling
– magnetosphere, 1
moments, 2
monopole potential, 6
monotonicity, 6
multi-fluid, 16

NENL, 14
neutral density, 9
neutral wind, 9
NmF2, 9
numerical diffusion, 6
numerical dispersion, 6
numerical flux, 5

parallel potential drop, 8
parallelization, 2
particle injection, 11
phase space, 2
physical flux, 5
plasma beta, 3
plasma sheet, 2, 10
Poisson equation, 6
potential equation, 7
projection method, 6

RCM, 16
reaction
– chemical, 9
– photo-chemical, 9
reconnection, 9, 10
resistivity
– anomalous, 3, 10
– numerical, 3
Rice Convection Model, 16
ring current, 2, 15

SAMR, 2
scheme
– first order, 6
– fourth order central, 5
– Godunov, 5
– Lax, 5, 6
– Lax Wendroff, 5
– leap-frog, 4
– predictor-corrector, 4
– Rusanov, 5, 6
– second order central, 5
– Van Leer, 6
solar wind, 9
space weather, 9, 12, 14
– forecasting, 12
spatial discretization, 5
spectral, 5
storm
– Bastille Day, 12
– geomagnetic, 12, 15
structured adaptive mesh refinement, 2
substorm, 10
– challenge, 1
– expansion phase, 10
– growth phase, 10
– onset, 10

tail dynamics, 10
TEC, 9
thermosphere, 1, 8
time differencing, 4
total electron content, 9
Total Variance Diminishing, 6
TVD, 6

UCLA code, 2

vector potential, 7

x-line, 11